Modeling of Electric Arc Furnaces (EAF) with electromagnetic stirring

Niloofar Arzpeyma

Supervisors:
Pär Jönsson and Ola Widlund

Master Degree Project

School of Industrial Engineering and Management
Department of Materials Science and Engineering
Royal Institute of Technology
SE-100 44 Stockholm
Sweden

Stockholm 2011

ABSTRACT

The influence of electromagnetic stirring in an electric arc furnace (EAF) has been studied. Using numerical modeling the effect of electromagnetic stirring on the thermal stratification and fluid flow has been investigated. The finite element method (FEM) software was used to compute the electromagnetic forces, and the fluid flow and heat and mass transfer equations were solved using a finite volume method (FVM) software. The results show that electromagnetic stirring has a significant effect on temperature homogenization and mixing efficiency in the bath. The important part of this study was calculation of heat transfer coefficient. The results show, electromagnetic stirring improves the heat transfer from the melt to scrap which is dependent on the stirring direction and force magnitudes.

ACKNOWLEDGMENTS

I would like to thank Prof. Pär Jönsson who provided me the opportunity to start this thesis, and Dr. Anders Tilliander and Mikael Ersson who always supported me.

I would like to gratefully acknowledge my supervisor in ABB, Dr. Ola Widlund, who always supervised me patiently and gave me support and confidence.

CONTENTS

Chapter 1

INTRODUCTION

Electric arc furnace has developed significantly over the past 30 years. Today, electrode and electric power consumption and tap to tap times are reduced considerably, as shown in Figure 1-1 [1, 2, 3].

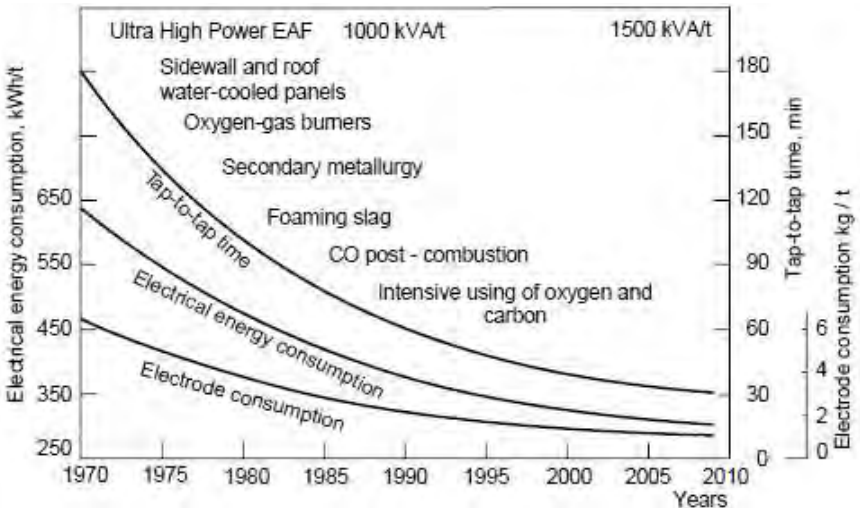

Figure 1-1. Developments in EAF performances [3].

However, further improvements in productivity and energy efficiency are required by acquiring a fundamental understanding of the process. Physical and computational fluid dynamic models contribute to obtain this understanding and improve it.

1.1 Purpose

When modelling the EAF, there are three areas of interest:

- The electromagnetic phenomena, heat transfer and fluid flow in the arc region.
- The fluid flow and temperature distribution in the bath.

- The heat and momentum transfer between arc and bath region.

In this study, computational fluid dynamic (CFD) has been used to study the influence of electromagnetic stirring (EMS) in scrap melting and transport phenomena inside the bath in an eccentric bottom tapping (EBT) EAF; in fact, using a three dimensional transient model, fluid flow, heat transfer and mixing phenomena, with and without EMS have been studied. For the case without stirring, natural convection was considered as the only driving force for momentum, and for EMS, different directions and force magnitudes were considered. Heat transfer coefficient was calculated to show the influence of stirring on scrap melting.

Chapter 2

BACKGROUND

2.1 Electric arc furnace

In steel industry, integrated steel mill and electric arc furnace (EAF), referred to as mini-mill, are two steel production routes. In integrated mill, iron ore is the primary raw material which is charged to blast furnace (BF), whereas mini-mill is charged by almost 100% scrap. EAFs rapidly evolved due to their lower production costs, lower impact on the environment and lower price of raw materials in comparison to the blast furnaces [1].

In addition to scrap, the EAF is charged by direct-reduced-iron (DRI) and fluxes. The main heat source in EAF is electric arcs formed between electrodes and bath. Heat is transferred to the bath through four mechanisms, convection, radiation, Thompson effect and condensation of electrons. Oxy fuel burners, post-consumption of CO and chemical reactions are other heat sources in EAF [2, 3].

Depending on type of arc produced, two kinds of EAFs exist:

AC Electric Arc Furnace: In AC electric arc furnace, three arcs are generated between the graphite electrodes and the charge. In each half of one period, the cathode and anode alternate. In the positive polarity mode the electrode is cathode and the surface of the bath is anode and in the negative polarity mode is vice versa. [4]

DC Electric Arc Furnace: In DC electric arc furnace, the arc is generated between a single graphite electrode, cathode, and the bottom electrode working as an anode.

In traditional EAFs tapping was done by tilting the furnace, whereas modern EAF are equipped with eccentric bottom tapping (EBT) to minimize the amount of slag transferred to the ladle during tapping [5].

2.2 Heat transfer mechanisms in the bath

The heat transferred to the bath is generated by four mechanisms which are:

- Convective heat transfer

- Radiative heat transfer
- Thompson effect
- Condensation of electrons.

The total heat transfer to the surface of the bath is defined as:

$$Q_0(r) = Q_R + Q_C + Q_E + Q_A = -k_{eff}\frac{\partial T}{\partial Z} \qquad (Eq. 2-1)$$

where k_{eff} is the effective thermal conductivity which is the sum of molecular and turbulent conductivities. The left hand side of the equation is the heat flux produced in the arc and is transferred to the bath surface which corresponds to the heat input into the melt, and is set as a heat flux boundary condition at the surface of melt, right hand side of the equation [4].

Gonzalez et al. [6] computed Q_0 as arc power P_0 by the Channel Arc Model (CAM) [7] for a certain power and arc length.

2.3 Melting in EAF

Scrap melting in iron – carbon melt has been investigated in both laboratory scales by melting specimens in small induction furnaces and in industrial furnaces using radioactive isotopes to track the melting process [3, 8]. One of the recent works was done by Li et al. [8, 9, 10] using phase-field model to study scrap melting process for a single and multiple steel bars.

2.3.1 Melting stages

The overall duration of the process can be divided into three main stages: [11]

Heating stage: The scrap is heated by the arc and oxy fuel burners at the top of the furnace. The heating is done by radiation, convection, due to the hot gas going through the scrap porosities and conduction, due to contact points between scraps. The temperature at the top increases to reach the melting temperature of the scrap. In this stage the gas – solid phases exist.

Melting stage: The melting starts at the top surface of the scrap pile, and molten liquid penetrate towards the bottom of the furnace and its height increases whereas the height of the scrap pile decreases. In this stage, there are gas – solid and solid – liquid phases in the bath.

Finishing stage: The scrap is completely covered by the melt and only the solid – liquid phase exists until all the scrap is melted.

Three regions shown in Figure 2-1 correspond to these three stages.

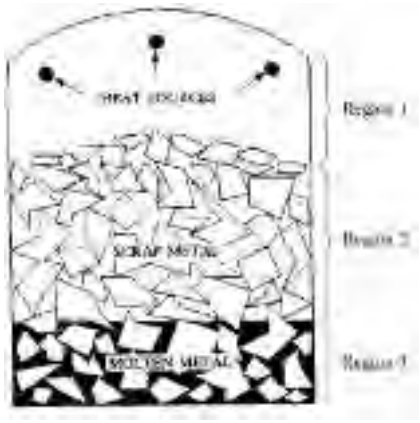

Figure 2-1. Three stages of scrap melting an AC EAF [11].

Scrap melting is a complicated process since both mass and heat transfer are involved. The process of scrap melting, when the scrap is immerged in the melt completely, can itself be divided into three stages from heat and mass transfer points of view, depending on the melt and scrap temperature and carbon content [3]:

First stage: Solidification of the melt. When the cold or preheated scrap is immerged into the bath, the melt around the surface of the scrap freezes and a solid crust, shell, is formed. First, the thickness of the shell increases rapidly. Then, by heating progress and increase of the scrap temperature, the growth rate decreases. The growth of the shell stops when the heat flux from the melt towards the surface of the shell is equal to the heat flux from the shell to the scrap, and the thickness of the shell is maximum. Then, the shell starts to remelt by rising the scrap temperature. It has been shown that the thickness of the shell and the time it exists are dependent on the size of scrap and temperature difference between melt and scrap.

Second stage: Diffusion melting. This stage occurs during melting of scrap in hot metal, when the melt temperature is lower than the scrap melting temperature. The carbon starts to diffuse from the melt into the surface of the scrap lumps, so the melting temperature of the surface layer becomes lower than the melt temperature.

Third stage: Intensive melting: this stage takes place when the melt temperature is higher than scrap melting temperature. The temperature difference and turbulent stirring, convection, in the bath contribute high rate of melting.

The first and second stages do not influence the melting rate significantly; the solidified shell is important only for the large scraps and carbon diffusion is a slow process, thus, the third stage determines the productivity of the furnace; that is, the high heat transfer is required to decrease tap – to – tap time.

2.4 Hot heel

Today, most of furnaces operate with the condition called "hot heel", meaning that almost 15–20 % of metal from the previous heat has remained at the bottom of furnace after tapping. Hot heel increases productivity by allowing use of high electric power since it decreases the possibility of damaging refractory by powerful arcs, and it also affects the melting rate of the scrap [3].

2.5 Foaming slag

At the start of the melting process, the arcs are covered by the scrap, so the radiation from the arcs to the lateral walls is low, but when the scrap starts melting, the heat efficiency decreases since the radiation to the walls increases. Thus, the foaming slag is used to cover the arcs as more heat can be transferred to the bath and scrap [3, 12].

Foaming slag is formed by injection of carbon and oxygen, shown in Figure 2-2. First, the carbon inside the bath is oxidized by oxygen blowing:[3]

$$C + \frac{1}{2} O_2 \rightarrow CO \qquad (Eq. 2-2)$$

Oxygen also oxidized certain amount of iron and FeO is formed. The carbon injected reduces iron oxide by reaction:

$$FeO + C \rightarrow Fe + CO \qquad (Eq. 2-3)$$

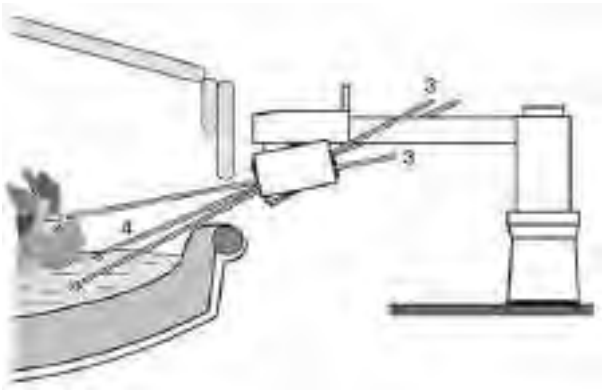

Figure 2-2. Oxygen (lance 4) and carbon (lance 3) injection [3].

These two reactions generate bubbles of CO which go upward and foam the slag.

Ramirez-Argaez et al. [13] used volume of fluid model to include the slag layer. They simplified the model by neglecting the heat transfer through the slag. The results show that the friction between slag and melt decreases the momentum

transfer in the melt compared to the case of free surface where the gas atmosphere is considered on the surface of the melt.

2.6 Bath circulation in EAF

2.6.1 stirring intensity

Stirring intensity has an important role on the physical and chemical processes in the bath. This parameter can be evaluated by the time during which the bath composition is homogenized in the whole bath after a tracer is introduced to the bath, such as copper or radioactive isotope of cobalt. The mixing time is determined by sampling from different points of the bath. This method of measuring stirring intensity, done when melting units are operating, is very expensive and complicated. The other option is use of physical models, but there are strict requirements to select both geometric and physical parameters respectively for the model and liquids representing the melt and slag [3]. Modelling based on numerical methods is another option to evaluate mixing phenomena using a scalar tracer in bath region [6].

2.6.2 Natural mechanisms

Observations show that the bath of EAF is circulated in a horizontal plane, the linear velocity of which is too low. However, due to the high density of the melt, the value of Reynolds number, Re, is high, indicating the turbulent motion in the bath [3]. Reynolds number is defined as:

$$Re = \frac{V.d}{v} \qquad (Eq.2-4)$$

where V is fluid velocity, m/s, d is the diameter of channel where the fluid flows, m, and v is kinematic viscosity of fluid, m^2/s.

In EAF, there are a number of driving forces generating turbulence in the bath and influence the melting rate and temperature distribution:

2.6.2.1 CO bubbling

CO is produced during decarburization in the bath by two reactions, mentioned in section 2.5, which contribute not only to slag foaming generation but also bath circulation [3, 6].

It has been confirmed that with increase of decarburization rate, corresponded to the number of CO bubbles, the stirring intensity of bath increases [3].

2.6.2.2 Electromagnetic forces (Lorentz forces)

The current density and the magnetic flux density in the arc region contribute to Lorentz force defined as:

$$F = J \times B \qquad Eq.(2-5)$$

Axial current density generates azimuthal magnetic field and radial current density generates radial magnetic field. Since the axial current density in the arc is much greater than the radial current density, only the azimuthal magnetic field is considered. Thus, using a two dimensional axis - symmetric system, the axial and radial components of the Lorentz force are written as:

$$F_z = J_r B_\theta \qquad (Eq.2-6)$$

$$F_r = -J_z B_\theta \qquad (Eq.2-7)$$

Maxwell's equations are used to describe the magnetic field in EAF [14]. Passage of current from electrodes to the bath generates an electromagnetic force which can contribute to bath circulation [4, 15].

2.6.2.3 Shear stress

Arc column, generated by the graphite electrode, impinges on the bath, and leads to generation of shear stresses at the top surface which is specified as:

$$\tau_{(r)} = \mu_{eff} \frac{dv_r}{dz} \qquad (Eq.2-8)$$

$$\mu_{eff} = \mu + \mu_t \qquad (Eq.2-9)$$

where $\tau_{(r)}$ is the shear stress generated by the arc in two-dimensional cylindrical coordinate system, μ is the molecular dynamic viscosity and μ_t is the turbulent dynamic viscosity.

The shear stress has a significant influence on the velocity distribution at the center of the surface of the bath due to transfer of jet momentum [4, 15, 16]. The studies having done on a DC electric arc furnace show that the value of the shear stress at the center of the bath surface, anode region is relatively low and, moving towards the walls, it increases to a maximum value and then decreases. Figure 2-3 shows the radial distribution of shear stress at half part of the surface.

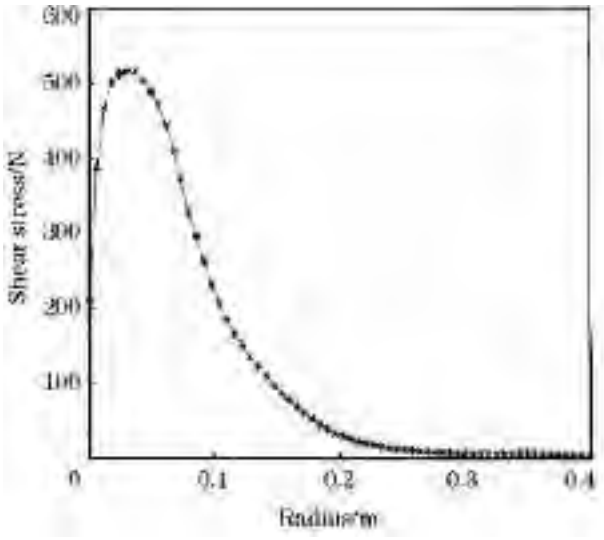

Figure 2-3. Shear stress at anode in DC EAF [15].

2.6.2.4 Natural (Free) convection

In contrast to the forced convection, in which an external driving force produces circulation, natural convection flow results from the heat transfer inside the bath; in fact, temperature variation in the bath causes a variation in density, resulting in a buoyancy force due to body force field [17, 18]. The body force, F, varies as ϱg for a gravitational field; thus, the variation of density, ϱ, with temperature, contributes to the fluid flow, and this variation is included in conservation equations when considering natural convection. The momentum equation for constant viscosity and zero bulk viscosity is written as: [18]

$$\frac{\partial(\rho\vec{V})}{\partial t} + \nabla.(\rho\vec{V}\vec{V}) = -\nabla P + \nabla.(\bar{\bar{\tau}}) + \vec{F} \qquad (Eq.2-10)$$

where P is the static pressure, $\bar{\bar{\tau}}$ is the stress tensor and F is body force.

Considering buoyancy forces, the static pressure, p is broken down to p_a, hydrostatic pressure and p_d, dynamic pressure due to the fluid flow as $p=p_a+p_d$. P_a is coupled with the body force, F, and produces buoyancy force which is the driving force for the flow, so: [18]

$$F - \nabla P = (\rho g - \nabla P_a) - \nabla P_d = (\rho g - \rho_\infty g) - \nabla P_d = (\rho - \rho_\infty)g - \nabla P_d \qquad (Eq.2-11)$$

where ρ_∞ is the fluid density in ambient medium.

Since g is downward, it is written as $\vec{g} = -gk$, where k is the unit vector in the z direction which is upward, then:

$$F - \nabla P = (\rho_\infty - \rho)gk - \nabla P_d \qquad (Eq.2-12)$$

The momentum equation, Eq. 2-10, becomes:

$$\frac{\partial(\rho\vec{V})}{\partial t} + \nabla.(\rho\vec{V}\vec{V}) = (\rho - \rho_\infty)g - \nabla P + \nabla.(\bar{\bar{\tau}}) \qquad (Eq.2-13)$$

Figure 2-4 shows a cross sectional view of a cylinder containing fluid and heated at the center of the upper surface. It is shown that two circulation loops are generated due to natural convection as the fluid flows downward close to the walls and upward at the center of the cylinder [4, 19]. It is shown that the maximum temperature corresponds to the boundary between two loops [19].

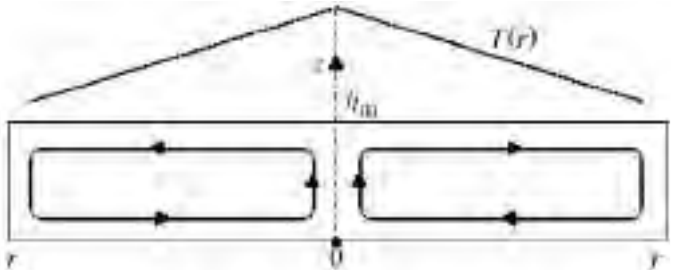

Figure 2-4. Diagram of the natural convection flow [19].

2.6.2.4.1 Boussinesq approximation [18, 20, 21]

The governing equations used for natural convection are very elaborate since they are coupled, elliptic and partial differential equations; in addition, the variation of density with temperature is unavoidable. Therefore, these equations are generally simplified using approximations among which the Boussinesq approximation is an important one. In the Boussinesq approximation, first, in the continuity equation (Eq.2-14) the density variation is neglected, so it changes to Eq. 2-15:

$$\frac{D\rho}{Dt} = \frac{\partial\rho}{\partial t} + V.\nabla\rho = -\rho\nabla.V \qquad (Eq.2-14)$$

$$\nabla.V = 0 \qquad (Eq.2-15)$$

Second, the density variation, the driving force for the flow, with temperature difference is assumed linear, so the thermal buoyancy is:

$$\rho_\infty - \rho = \rho\beta(T - T_\infty) \qquad (Eq.2-16)$$

where β is the thermal expansion, and this approximation is valid for $\beta(T - T_\infty) \ll 1$,

and the buoyancy force is expressed as:

$$F_b = -g\rho\beta(T - T_\infty) \qquad (Eq.2-17)$$

2.6.3 Bath circulation in DC EAF

In a DC EAF, electrons transfer from the graphite electrode to the bottom electrode, so it contributes to a strong electromagnetic body forces generated in the steel bulk. Wang et al. [15] investigated bath circulation in a DC electric arc furnace having one bottom electrode. The velocity distribution is presented in Figure 2-5. The two vortices at the left side of the figure are due to electromagnetic forces. The vortex at the right and top surface of the bath is due to buoyancy and radial shear stress. The electromagnetic forces are higher than buoyant force and shear stress, and they are also much higher at the surface of the bath.

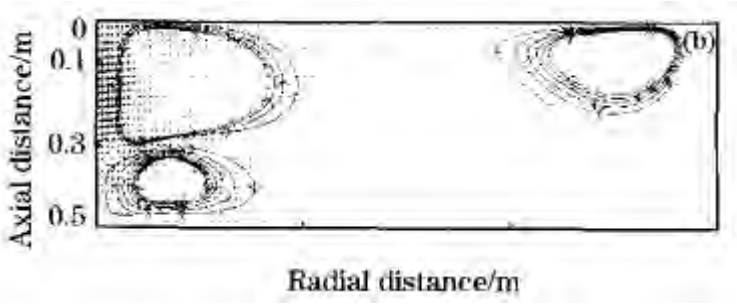

Figure 2-5. Velocity distribution after 5 s [15].

2.6.4 Bath circulation in AC EAF

In contrast to the DC electric arc furnace, in AC EAF, there is no anode electrode at the bottom of the furnace, so the currents from the graphite electrodes are concentrated on the top surface of the bath [6]. F. David et al. [14] evaluated the electromagnetic field in the AC electric arc furnace using Maxwell's equations. The radial, axial and tangential Lorentz force density and the Joule power density were estimated in the molten steel for cases with and without foaming slag. The results show that the force density, having the same pattern for both cases, is very non uniform and acts close and between the electric arcs. In fact, in AC electric arc furnace the electromagnetic field induced is limited to the regions around the arcs and can be neglected as a driving force for the flow [14, 20].

Szekely et al. [4] investigated jet momentum and buoyancy as driving forces for the bath circulation in a cylindrical DC furnace (2 m diameter and 18 MW arc power), but the circulation due to electromagnetic forces were neglected. Figure 2-6 shows the velocity distribution in the bath for the case with both mechanisms (case 1) and the case with only natural convection (case 2). The figures show a clockwise circulation in the bath with the highest radial velocity near the arc where, for the case 1, see Figure 2-6 (a), the linear velocity is almost 0.2 ms^{-1} and is considerably lower and about 0.006 ms^{-1} for the case 2, see Figure 2-6 (b).

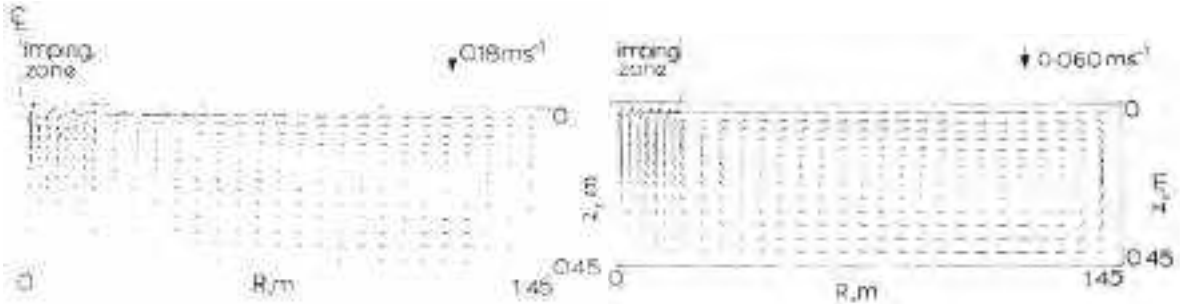

(a) (b)

Figure 2-6. Velocity distribution in the bath due to the buoyancy and jet momentum (a) and buoyancy (b) [4].

Figure 2-7 shows the results of temperature distribution only for the case 2. It shows that there are thermal gradients near the surface and the impinging region, Figure 2-7, and they show that temperature is less uniform for the case 2 since the convection is reduced when the jet momentum is not considered.

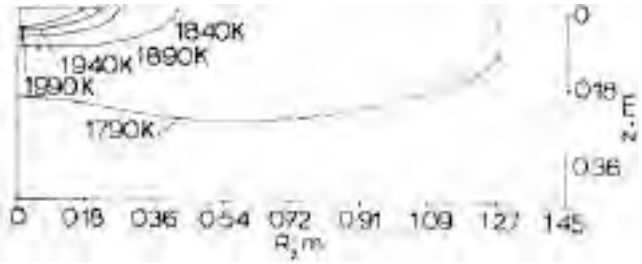

Figure 2-7. Temperature distribution in the bath due to the buoyancy [4].

Gonzalez et al. [6] investigated the velocity and temperature fields resulting from natural convection in an AC electric arc furnace (8 m diameter and 120 MW arc power). Figure 2-8 and 1-9 shows the cross sectional view of the velocity and temperature distribution respectively. It has been shown that three temperature zones are formed in the bath, cold zone, hot zone and superheated zone.

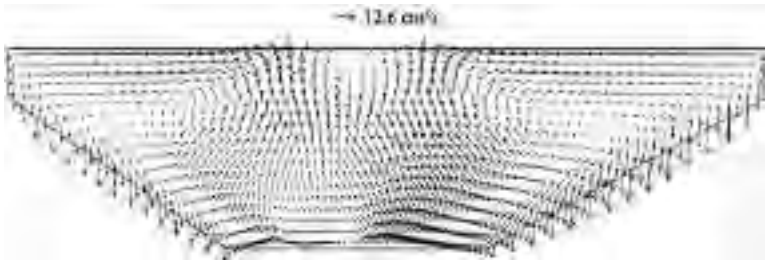

Figure 2-8. Velocity fields, cross view [6].

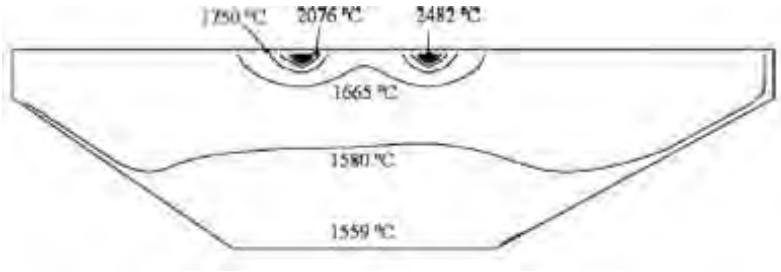

Figure 2-9. Temperature fields, cross view [6].

Li et al. [8] included scraps in the bath and used the phase-field model [9] to simulate melting. They considered the case when there is no forced convection in the bath, and the large pieces of scrap were widely distributed in the melt. The results showed higher melting time in comparison to the case when there was forced convection in the bath.

2.6.5 Stirring (forced convection)

As mentioned, the melt can flow due to mechanisms taking place during the melting process, but thermal stratification does not disappear, so it will take a long time for large pieces of scrap to be melted. Concentration gradient in the bath has also been reported which causes the reaction rates in the bath to decrease and also the reactions do not take place uniformly in all parts of the bath [2].

Thermal stratification is a more common problem in ultra-high power (UHP) furnaces where there is a high superheat. Thus, it is important that the melt dripping down from the top is convected to reduce stratification [8].

Therefore, the idea of stirring or forced convection in the bath was introduced years ago to improve the melt flow and eventually decrease the energy consumption. The first electromagnetic coils were used in a laboratory scale in 1933, and the studies showed that the flow velocities for stainless steels are lower than carbon steels when electromagnetic stirring was used [2].

It has been shown that stirring is more important in production of low carbon steels since when the content of carbon goes down to below 0.2 %, decarburization due to oxygen blowing is not that effective; thus, a powerful driving force is required to transfer carbon to the reaction zone, where oxygen is blowing [3].

In forced convection, an external driving force is used to make the fluid flow, and the magnitude of velocity and rate of heat transfer increase in comparison to the natural convection.

The profile of melting for solid steel is shown in Figure 2-10. Through the interface of the solid and the melt, boundary layer, and also inside the solid, the heat is transferred by conduction. The boundary layer, δ_T, is defined as a distance from the solid surface to the point where temperature is 99 % of liquid temperature. T_0 is the initial temperature of

steel, T_l is liquid temperature and T_m is melting temperature which is the interface temperature after immersion of steel in the melt [9].

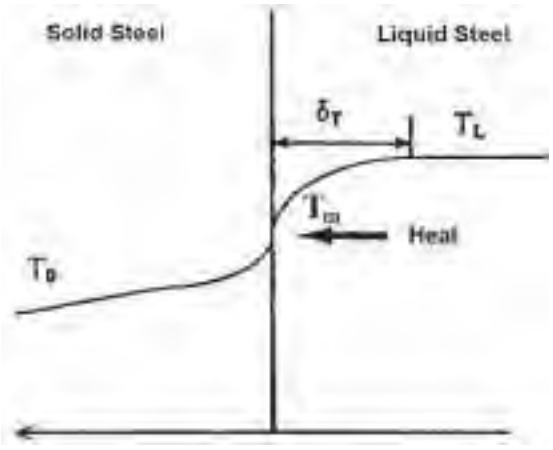

Figure 2-10. Temperature profile of steel melting in melt [9].

Thus, when the fluid velocity increases, the thickness of the stationary fluid surrounding the solid, the boundary layer, decreases, so the heat transfer at the solid surface can be improved. It has been shown that the coefficient of this layer increases as (fluid velocity)^n, where n, depending on the geometry, is varied between 0.6 and 0.8 [17].

2.6.5.1 Heat transfer coefficient

The convective heat transfer between fluid and solid is a complicated process, and it depends on many factors such as physical properties of the fluid, changing with temperature, shape and size of interface, and also the motion of the fluid. The convective heat transfer is simplified using Newton's law where the amount of heat Q transferred from a fluid to a solid surface or vice versa is proportional to the temperature difference between fluid, T_l , and surface, T_s , and the area, A, in which heat transfer takes place, so: [3]

$$Q = hA(T_1 - T_2) \qquad (Eq. 2-18)$$

where h is the coefficient of proportionality and is called heat transfer coefficient, and represents intensity of the heat transfer process. $\frac{1}{h}$ can be considered as the thermal resistance in the film between fluid and the solid surface [17]; in fact, the heat transfer coefficient gathered all complexity of the convective heat transfer phenomena and is dependent on the factors mentioned above.

The results of studies on heat transfer in turbulent fluids led to three dimensionless numbers: the Reynolds number, described insection 1.6.2, the Nusselt number Nu:

$$Nu = \frac{h.d}{k} \qquad (Eq. 2-19)$$

,and the Prandtl number *Pr*:

$$Pr = \frac{c_p . \rho . v}{k} \qquad (Eq. 2-20)$$

where k is thermal conductivity and c_p is specific heat capacity.

The Nusselt number for the case forced convection is reported as: [22]

$$Nu = C . Re^n . Pr^{\frac{1}{3}} \qquad (Eq. 2-21)$$

where *C* and *n* are calculated by experimental data.

Some investigations have been done in steelmaking industry to measure the heat transfer coefficient and reach a correlation between Nusselt number and Reynolds number. The following is the results obtained or the values used to study the scrap melting process in different conditions.

Szekely et al. [23] studied the melting process of a relatively low carbon scrap bars in a melt with a higher carbon content. Considering both mass and heat transfer, they reported the values between 3,500 and 11,800 W/m^2.K for heat transfer coefficient. Gaye et al. evaluated heat transfer coefficient as a function of the input energy to the furnace (see Eq. 1-22), so the effect of blowing was involved. They reached the values between 17,000 and 50,000 W/m^2.K. [22, 24]

$$h = 5000 \varepsilon^{0.2} \qquad (Eq. 2-22)$$

The correlation suggested by Kreith for a horizontal cylinder which is exposed to a perpendicular flow to its axis is expressed as: [22]

$$Nu = 0.0266 . Re^{0.805} . Pr^{\frac{1}{3}} \qquad for\ 40{,}000 < Re < 400{,}000 \qquad (Eq. 2-23)$$

The value that Li et al. [15] used to study gas stirring for scrap bar melting was 13,000 W/m^2.K. Enrich et al. [22, 24, 25] studied the melting of scrap spheres for both dense and sponge irons. A numerical procedure called Green's function was used assuming that the melt is stirred by electromagnetic forces. They used the value 25,000 W/m^2.K for the heat transfer coefficient.

The studies show that the heat transfer coefficient resulted due to the forced convection in the bath is much higher in comparison to values for natural convection.

Two methods of stirring using to improve heat transfer in EAF are bottom gas stirring and electromagnetic stirring.

2.6.5.2 Bottom gas injection

As mentioned in section1.6.2.1, CO bubbles, formed during formation of the foaming slag, contribute to bath circulation, but an additional amount of gas can be injected into the bath to increase the intensity of bath stirring. Inert gas, argon, nitrogen or mixture of both can be injected through tuyeres or porous plugs submerged within the bottom refractory of the furnace. The number of tuyeres or plugs used is dependent on their size as well as the size of the furnace. The blowing is usually done with the low intensity of 0.1 m^3/ton.min [2, 3].

The investigations done by Irons et al. [6] on the melt flow due to bottom gas injection, oxygen injection and CO formation shows that stirring is not completely uniform over the bath. They have also found that stirring is increased when CO is trapped into the argon bubbles, and the maximum velocity vector reported was 1.52 $m.s^{-1}$.

Caffery et al. [20] used CFD modelling to study temperature homogenisation in the EBT region of EAF due to top lance and bottom bubbling. The results showed the interaction between top lance and bottom stirring contribute to temperature homogenisation, but they reported that when the gas flow rate increases to 5 Nm^3/h, a stagnant cold zone still exists.

The results of modelling done by J. Li et al. [8] also showed that bottom gas injection reduces temperature stratification, but it cannot eliminate it.

El- Kaddah et al. [26] studied the velocity fields in a 6 ton ladle stirred by argon injection through a plume at the bottom. The results showed the maximum velocity takes place at the jet plume and free surface, while other parts of the bath remain relatively stagnant.

Some companies reported the saving energy 10 to 30 kWh/ton steel achieved by bottom stirring which brings the melt from the top to the bottom leading to a lower melting time [8].

It has been shown that bottom gas stirring is more useful in ladle furnaces to increase mixing and temperature homogenisation [27, 28, 29] but, in EAF, since the ratio of height to diameter is low, it is less efficient [6].

2.6.5.3 Electromagnetic stirring

Electromagnetic (Lorentz) force was introduced in 2.6.2.2. Electromagnetic forces can contribute to circulation in AC EAF by electromagnetic stirrer installed at the bottom of the electric arc furnace, EAF EMS, which is shown in Figure 2-11. The first commercial installation of this technology was at Uddeholm AB in Hagfors, Sweden. By development of ladle furnace in which the secondary processes are done, installation of EMS was stopped in 1983 [30]. However, today, that EAFs operates with larger heel sizes, electromagnetic stirring can increase the convection significantly, and it improves the scrap melting process and reduces tap to tap times significantly [8].

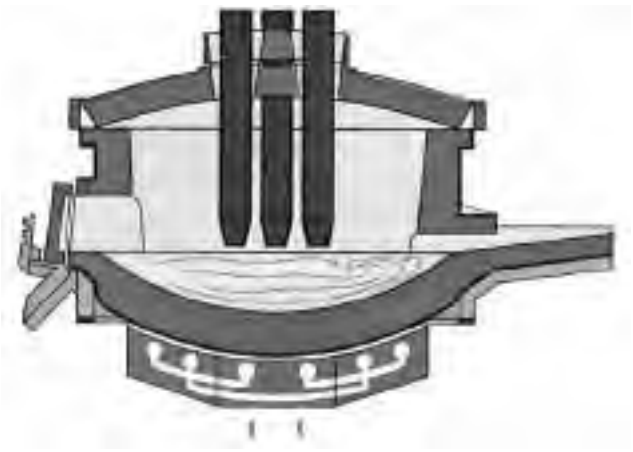

Figure 2-11. Electromagnetic stirrer placed at the bottom of an AC EAF.

David et al. [14] investigated two cases of electromagnetic stirring in an AC EAF:

- DC electromagnetic stirring with four bottom electrodes, and also an extra central electrode and an external coil.
- AC electromagnetic stirring with two pairs of opposite electrodes supplied by two currents $i = \sqrt{2}\, I \sin\omega t$ and $i = \sqrt{2}\, I \cos\omega t$ and low frequency.

The results were presented as radial, axial and tangential Lorentz force density in the bath. In the case 1, when there were only four electrodes, the axial force density, F_z, has high values in the zones between the electrodes having similar polarity. The radial force, F_r, has the positive values in the vicinity of the electrodes and negative values in the zones between the electrodes having the same polarity. The tangential force, F_0, is almost zero. Thus, to have a better circulation, a central electrode and an external coil were used. The results show that the tangential force is more dominant leading to significant circulation in the bath. In the case 2, the values for the axial and radial forces are more significant than the tangential force.

Comparison between bottom gas stirring and electromagnetic stirring in a 6 ton ladle showed that using gas stirring, the high velocity is concentrated at gas jet region, whereas with electromagnetic stirring, the turbulent kinetic energy is relatively high in all parts of the bath and there is no stagnant zone [26].

Chapter 3

MATHEMATICAL MODELLING

Computational fluid dynamics, CFD, plays a significant role in engineering prediction. It complements pure experiment and pure theory, and is applied to solve partial differential equations which describe the fluid flow and heat and mass transfer. The commercial CFD package, FLUENT software version 13.0.0 was used to solve the equations, finite element method software OPERA was used to compute electromagnetic forces.

3.1 Governing equations

Mass, momentum and energy conservations are fundamental physical principles for all fluid flows. The following equations were solved during modeling:

3.1.1 Mass conservation

The equation of continuity is expressed as:

$$\frac{\partial \rho}{\partial t} + \nabla.(\rho \vec{V}) = S_m \qquad (Eq.3-1)$$

where S_m is the source term which is zero in our case.

3.1.2 Momentum conservation

Momentum conservation is based on the Newton's second law

As mentioned in 1.6.2.4, for the case natural convection the momentum equation is written as:

$$\frac{\partial (\rho \vec{V})}{\partial t} + \nabla.(\rho \vec{V}\vec{V}) = (\rho - \rho_\infty)g - \nabla P + \nabla.(\bar{\bar{\tau}}) \qquad (Eq.3-2)$$

For the case with electromagnetic stirring, the Lorentz force, F, is added as an external body force:

$$\frac{\partial (\rho \vec{V})}{\partial t} + \nabla.(\rho \vec{V}\vec{V}) = (\rho - \rho_\infty)\vec{g} - \nabla P + \nabla.(\bar{\bar{\tau}}) + F \qquad (Eq.3-3)$$

During melting an addition source term will be added to the momentum equation due to changes in liquid fraction, see Eq.3-11.

3.1.3 Energy conservation

To model scarp melting, the energy equation was solved after 200 s of starting simulation. The delay was to establish a developed flow. For melting the energy equation is written as:

$$\frac{\partial(\rho H)}{\partial t} + \nabla.\left(\rho\vec{V}H\right) = \nabla.(k\nabla T) + S \qquad (Eq.3-4)$$

where H is enthalpy, ρ is density, $\vec{V}$ is melt velocity and S is source term.

3.1.4 User-defined scalar (UDS) transport equation

One additional transport equation was used to detect mixing efficiency in the bath. For an arbitrary scalar φ_k the following transport equation is solved:

$$\frac{\partial \rho\varphi_k}{\partial t} + \frac{\partial}{\partial x_i}\left(\rho u_i\varphi_k - \Gamma_k\frac{\partial\varphi_k}{\partial x_i}\right) = S_{\varphi K} \qquad (Eq.3-5)$$

where $\Gamma_k\frac{\partial\varphi_k}{\partial x_i}$ is the diffusion term, Γ_k is diffusion coefficient, which was equal to 0.00001 and $S_{\varphi k}$ is the source term which was 0.

The UDS was initialized with a linear vertical profile as it was set to 0 and 1 at the bottom and top of the melt respectively, Figure 3-1. The UDS equation was solved after 300 s of starting simulation.

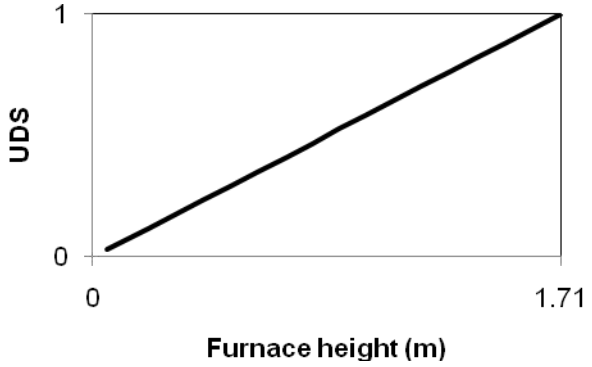

Figure 3-1. correlation between UDS and the furnace height.

3.2 Tool description

The simulation tool, called METALFURN is used to simulate electromagnetic properties of the stirrer, the melt flow, convective heat transfer in the melt and heat conduction through the walls and scrap melting. The functionality of METALFURN is provided by parameterized template models, and is based on FLUENT, flow solver, and OPERA software used for electromagnetic modeling.

The parameters have default values which can be changed for each case directory created in a model template. A script-based tool, called PARSIM, is used to manipulate simulation models.

3.3 Work flow

FLUENT 13.0.0, using finite - volume method (FVM), was used to solve conservation equations, and the software OPERA, using finite element method (FEM), was used to add electromagnetic forces to the momentum equation.

METALFURN was executed on a remote Linux cluster resource and PARSIM tool was used to create case directories and run FLUENT and OPERA in the Linux environment.

A parameter called FORCEMAG was used which is a scaling factor for the electromagnetic volumetric forces (N/m^3). FORCEMAG varies from 0, when there is no electromagnetic stirring to 1 when there is full stirring.

Two stirring directions, forward and backward, were studied. The force is applied in y direction towards the EBT region in forward stirring and is vice versa for backward stirring.

First, 9 case directories were created in a model template called EAF_SC, see Table 3-1.

The work flow has been described below in 5 steps and it is also summarized in Figure 3-2.

OPERA: OPERA geometry and FEM mesh are created.

FLUENT: a journal file is read containing:

Scheme variables which are the variables can be defined by users through the text interface in FLUENT executing a Scheme interpreter.

A command to read boundary conditions from a bc file,

A Scheme file which is read to execute grid refinement in the scrap region.

A user defined execute on demand file which is read for the temperature and UDS initialization.

A command to create a file containing the cell-center coordinates of the FLUENT mesh which will be used for force interpolation from OPERA into FLUENT.

Finally a case and date files are created, called init1.

OPERA: electromagnetic forces are interpolated into cell centers of FLUENT mesh and they are stored in a file.

FLUENT: a journal file is read containing:

A file containing forces called through a FLUENT user defined function (UDF), so the forces are read from OPERA and stored in user defined memories.

Finally a case and data files are created called init2.

FLUENT: The simulation is done by reading a journal file containing commands to read init2 case and data files and execute solver settings and run simulation.

Table 3-1. The case directories created for different stirring conditions and forces, R=0.15 m

FORCEMAG / Stirring condition	0	0.25	0.5	0.75	1
Forward		Case 1	Case 2	Case 3	Case4
Backward		Case 5	Case 6	Case 7	Case8
Without stirring	Case 9				

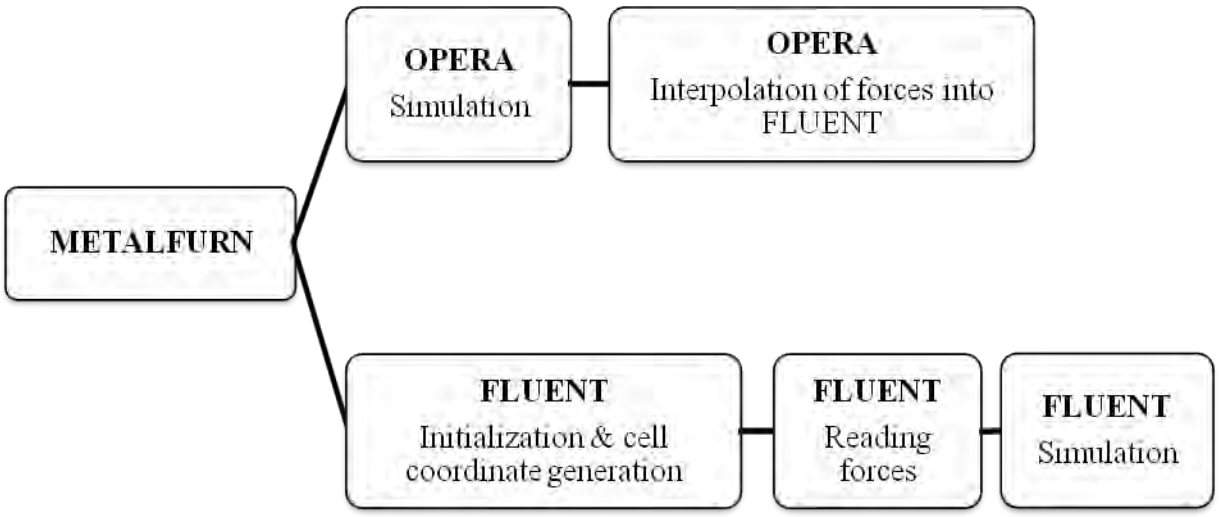

Figure 3-2. Work flow.

3.4 Models

3.4.1 Realizable k – ε model

The Realizable k – ε model was used to calculate turbulent viscosity since using Reynolds Stress Model (RMS), the convergence was not achievable. In this model, two transport equations are solved for turbulent kinetic energy k and dissipation of turbulent kinetic energy ε as:

$$\frac{\partial}{\partial t}(\rho k) + \frac{\partial}{\partial x_j}(\rho k u_j) = \frac{\partial y}{\partial x_j}\left[\left(\mu + \frac{\mu_t}{\sigma_k}\right)\frac{\partial k}{\partial x_j}\right] + G_k + G_b - \rho\varepsilon + S_k \qquad (Eq.3-6)$$

$$\frac{\partial}{\partial t}(\rho \varepsilon) + \frac{\partial}{\partial x_j}(\rho \varepsilon u_j) = \frac{\partial}{\partial x_j}\left[\left(\mu + \frac{\mu_t}{\sigma_\varepsilon}\right)\frac{\partial \varepsilon}{\partial x_j}\right] + \rho C_1 S_\varepsilon - \rho C_2 \frac{\varepsilon^2}{k + \sqrt{v\varepsilon}} \qquad (Eq.3-7)$$

$$+C_{1\varepsilon}\frac{\varepsilon}{k}C_{3\varepsilon}G_b + S_\varepsilon$$

where u_j is velocity magnitude, $C1$ is defined in FLUENT User's Guide [21], C_2 and C_ε are constant and equal to 1.9, σ_k and σ_ε are respectively turbulent Prandtl numbers for k and ε and equal to 1 and 1.2, S_ε and S_k are user defined source terms which were 0, and G_k and G_b are generation of turbulence kinetic energy due to the mean velocity and buoyancy respectively.

μ_t is defined as a function of k and ε as:

$$\mu_t = \rho C_\mu \frac{k^2}{\varepsilon} \qquad (Eq.3-8)$$

where C_μ is a function of mean strain and rotation of the fluid, so it prevents unrealizable values for the normal stresses and is defined as:

$$C_\mu = \frac{1}{A_0 + A_s \frac{kU^*}{\varepsilon}} \qquad (Eq.3-9)$$

The parameters are defined in FLUENT User's Guide [21].

3.4.2 Solidification and melting model

In FLUENT, an enthalpy – porosity method is used for modeling solidification/melting. In this model, the quantity indicating the fraction of the cell volume in liquid form, called liquid fraction, β, is associated with each cell in the domain. At each iteration, the liquid fraction is computed based on an enthalpy balance. The liquid fraction defined as:

$$\beta = 0 \qquad if\ T < T_{solidus}$$

$$\beta = \frac{T - T_{solidus}}{T_{liquidus} - T_{solidus}} \qquad if\ T_{solidus} < T < T_{liquidus} \qquad (Eq. 3-10)$$

$$\beta = 1 \qquad if\ T > T_{liquidus}$$

The region in which liquid fraction ranges between 0 and 1 is called mushy zone which is modeled as pseudo porous medium, and the porosity, which, in each cell is equal to the liquid fraction in that cell, ranges from 0 to 1 and the velocity also increases from 0 during melting.

3.4.2.1 Momentum equation

Thus, during melting, the momentum sink is added as the following term, *S*:

$$S = \frac{(1-\beta)^2}{(\beta^3 + \varepsilon)} A_{mush} (\vec{V} - \vec{V}p) \qquad (Eq. 3-11)$$

where ε is a small number, 0.001, A_{mush} is the mushy zone constant, 100000, and $\vec{V}p$ is the pull velocity which was not included in our simulation, so:

$$S = \frac{(1-\beta)^2}{(\beta^3 + \varepsilon)} A_{mush} \vec{V} \qquad (Eq. 3-12)$$

3.4.2.2 Turbulence equations

Sink terms are also added to turbulence equations in the mushy and solidified regions:

$$S = \frac{(1-\beta)^2}{(\beta^3 + \varepsilon)} A_{mush} \emptyset \qquad (Eq. 3-13)$$

Where ϕ is the turbulence quantities, k and ε.

3.4.2.3 Energy equation

The sum of the sensible enthalpy, h, and the latent heat, ΔH gives the enthalpy of the material, H:

$$H = h + \Delta H \qquad (Eq. 3-14)$$

where

$$h = h_{ref} + \int_{T_{ref}}^{T} c_p \, dT \qquad (Eq. 3-15)$$

$$\Delta H = \beta L \qquad (Eq. 3-16)$$

and h_{ref} is reference enthalpy, T_{ref} is reference temperature, c_p is specific heat capacity, and L is latent heat of the material, given in Table 3-5.

The temperature is solved using energy conservation Eq. 3-4 and Eq. 3-15. Since using Eq. 3-15 directly to get liquid fraction leads to a poor convergence, the method proposed by Voller and Swaminathan, used in FLUENT.

3.5 Natural convection

The Boussinesq approximation was used to solve buoyancy driven flow and involve natural convection. In FLUENT, using this model, we can get faster convergence. T_∞ in Eq. 2-17 is the operating or reference temperature and ρ is the Boussinesq or reference density of the flow, given in Table 3-5. To include buoyancy, the gravitational acceleration was applied in z direction, - 9.81 m/s^2.

This model was applied for both cases with and without EMS.

3.6 Computational domain

3.6.1 Geometry and meshing of the melt

The computational domain was the 3 dimensional melt region of a hypothetical 150 ton electric arc furnace with eccentric bottom tapping (EBT), Figure 3-3. The arc spots on the melt surface were created using three circles. The parameters used to build the melt geometry are summarized in Table 3-2. The tetrahedral meshing with inflation was applied, and the number of cells was equal to 1,600,000, Figure 3-2. The geometry and meshing were created using ANSYS 13.0.0.

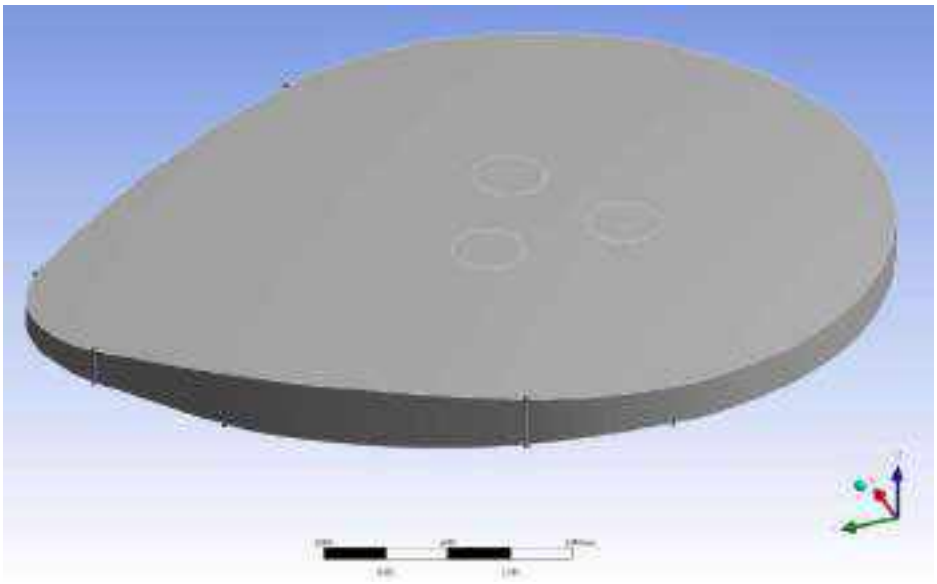

Figure 3-3. Geometry of the melt.

Table 3-2. The dimensions of the melt geometry.

Parameter	Volume	Large diameter	Diameter in EBT zone	Melt height	Arc spot radius	Length
Value	22.02	5.7	1.8	1.17	0.3	7.2
Unit	m^3	m	m	m	m	m

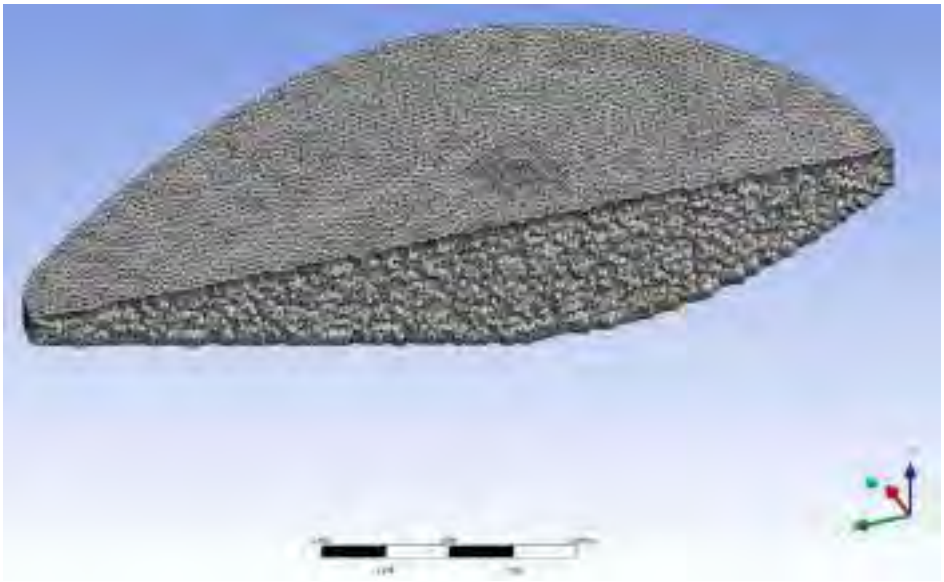

Figure 3-4. A symmetrical section of the meshed geometry.

3.6.2 Geometry and meshing of scrap

In FLUENT, the geometry of the scrap was initialized as a cylinder at the EBT zone using user defined function (UDF), Figure3-5. All cells inside the cylinder had the scrap temperature and zero liquid fraction. Three different radii were used.

Figure 3-5. The scrap modeled at the EBT zone with the radius 0.15 m at t = 0.

To have a higher resolution, the grid refinement was done in FLUENT to the third level in the scrap region, Figure 3-6, so the number of cells increased to 1,800,000. In Table 3-3, the dimensions used for the scrap and refinement region are given.

Table 3-3. The dimensions of the scrap geometry and refined region.

Parameter / Region	Radius 1	Radius 2	Radius 3	Cylinder axis length
Scrap region	0.1	0.15	0.2	0.14
Refined region	0.2	0.25	0.3	0.24
Unit	m	m	m	m

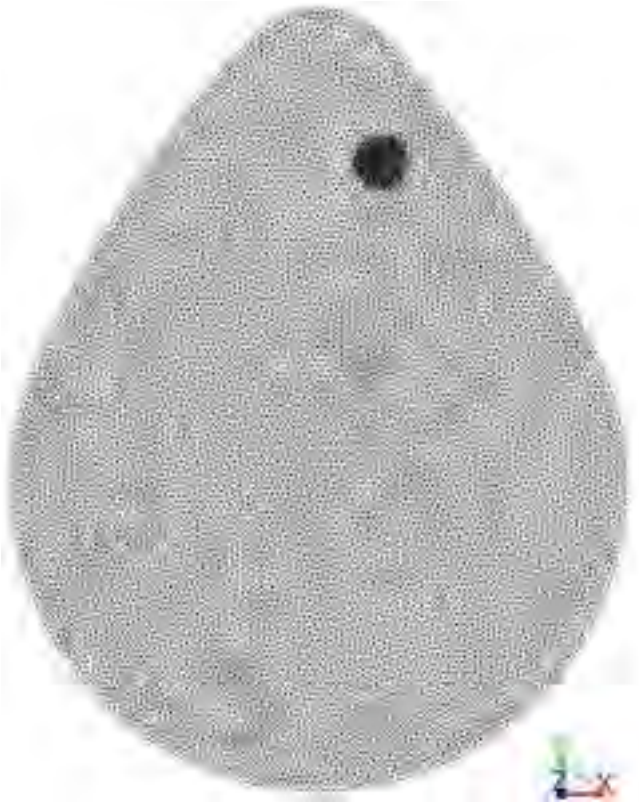

Figure 3-6. Grid refinement for the scrap zone; bottom surface of the melt geometry.

3.7 Boundary conditions

Figure 3-7 shows the boundary conditions applied in a cross sectional view of the schematic furnace.

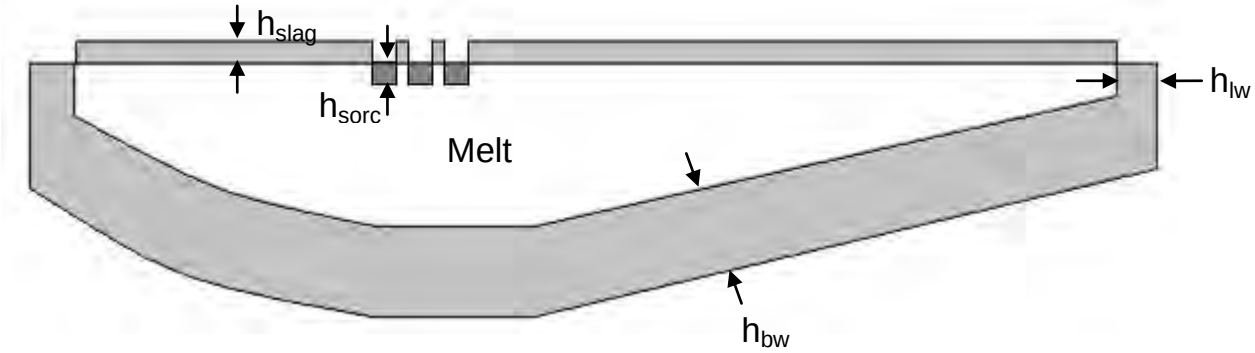

Figure 3-7. Boundary condition for slag and bottom and lateral walls.

3.7.1 Bottom and lateral walls

Shell conduction [21] was applied to model the solid bottom and lateral refractories. The wall thickness was defined according to the Table 3-4. When the wall thickness is not zero, thermal conduction is defined across the wall. Then since the heat is transferred from the external wall surface to the ambient medium by convection Q_c and radiation Q_r, the mixed thermal condition was used. The wall are stationary and the non slip condition

was applied to all walls, which means that the melt sticks to the wall and flow with the same velocity as the wall. The heat transfer coefficient for convection and external emissivity for radiation and ambient temperature have been brought in Table 3-5.

Table 3-4. Boundary condition parameters.

Boundary condition parameter	Value	Unit
Bottom wall thickness, h_{bw}	0.8	m
Side wall thickness, hlw	0.4	m
Slag thickness, h_{slag}	0.25	m
Source height, h_{source}	0.3	m

3.7.2 Slag

The slag layer was modeled explicitly. According to work done by Gonzalez [6], the gas atmosphere was adopted at the surface from which heat is transferred by radiation, but here the shell conduction was used to apply the slag layer as a stationary solid wall without slip. The mixed thermal condition was also applied. The slag thickness and heat transfer coefficient, external emissivity, and the external radiation and convection temperatures have been brought in Table 3-5. Since the heat transfer due to convection through the slag layer was neglected, by assuming the solid wall, it was assumed that the solid slag has a high thermal conductivity which can be representative of convective heat transfer through the slag layer.

3.7.3 Arcs

It was assumed that all heat applied by electric arcs is transferred to the melt through the arc spots, and there is no thermal dissipation due to radiation; thus, the heat flux corrosponds to the arc power was used as a boundary condition at three arc spots. This simplification of heat input was also found in other literatures [4, 6].

For the case of natural convection, it was necessary that the power was ramped up gradually to reach a robust convergence. Therefore, three volume sources were applied at the height of 0.3 m below the arc spots. The real heat flux through the arc spots is defined as:

$$\text{Real arc heat flux at the surface} = \frac{\text{Instant total arc power} - \text{Instant source power}}{\text{Arc area}}$$

Figure 3-6 shows the power changes vs. time and the two areas indicating the heat applied at the arc spots and inside the sources.

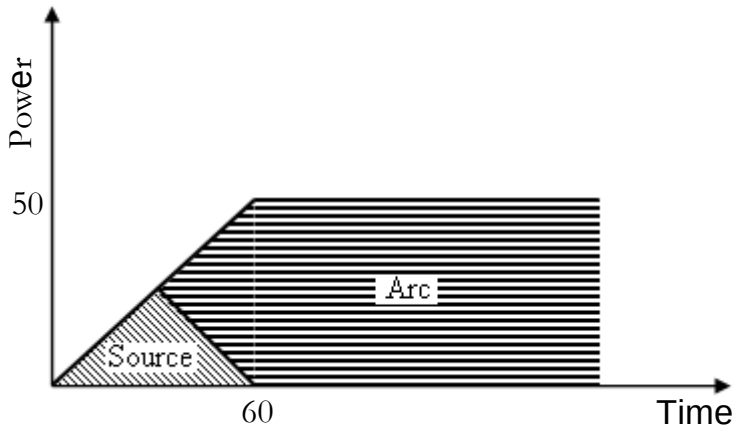

Figure 3-8. The source area indicates heat applied inside three volumes and arc area indicates heat applied at the arc spots.

3.8 Material properties

The properties used belong to low carbon steel, and it was assumed that steel and scrap have the same properties. The densities, specific heat capacities and thermal conductivities for all material were assumed to be constant. The properties for steel, slag and refractories are listed in Table 3-5.

Table 3-5. Properties of steel, slag and refractory used in simulation.

Model parameter	Value	Unit
Steel density	6900	kg/m^3
Steel specific heat capacity	792	J/kg.K
Steel viscosity	0.007	kg/m.s
Steel conductivity	35	W/m.K

Steel thermal expansion	0.0003	1/K
Steel latent heat	240000	J/kg
Refractory thermal conductivity	0.5	W/m.K
Slag thermal conductivity	80	W/m.K
Heat transfer coefficient outside of refractories	10	$W/m^2.K$
Ambient temperature	300	K
Freeboard temperature	1000	K
Initial melt temperature	1800	K
Arc power	50	MW

3.9 Solution methods

A pressure based solver and transient analysis were applied.

In monitor, the convergence criteria for continuity, x, y, and y velocity, k, ε and UDS were set to 10^{-4} and for energy was set to 10^{-7}.

In solution controls, the standard SIMPLE algorithm and the PERESTO! (PREssure Staggering Option) scheme were used for pressure discretization, recommended in FLUENT for natural convection. The default under relaxations for momentum, ε and k were reduced to 0.5, 0.4 and 0.4 respectively to stabilize the convergence.

In solution initialization, the values for k, ε and reference temperature were set to 0.001, 0.001 and 1900 respectively.

3.10 Performance indicators

3.10.1 Stirring power

Stirring power was calculated as a performance indicator of EAF EMS. The specific stirring power was calculated by mass weighted integral over the dissipation of the mechanical energy as:

$$\int \rho \varphi dV \qquad (Eq. 3-17)$$

where φ is the specific stirring energy which is defined as:

$$\varphi = 2\nu S_{ij} S_{ij} + 2\nu \overline{s_{ij} s_{ij}} \qquad (Eq. 3-18)$$

where ν is the kinematic viscosity, S_{ij} is the mean rate of strain:

$$S_{ij} = \frac{1}{2}\left(\frac{\partial U_i}{\partial x_j} + \frac{\partial U_j}{\partial x_i}\right) \qquad (Eq. 3-19)$$

And s_{ij} is the fluctuating rate of strain:

$$s_{ij} = \frac{1}{2}\left(\frac{\partial u_i'}{\partial x_j} + \frac{\partial u_j'}{\partial x_i}\right) = \varepsilon \qquad (Eq. 3-20)$$

Since the Reynolds number is very large, the fluctuating strain rate s_{ij} is thus very much larger than the mean rate of strain S_{ij}, so:

$$\overline{s_{ij} s_{ij}} \gg S_{ij} S_{ij} \qquad (Eq. 3-21)$$

The stirring power was also calculated by the integral over the dot product of force, N/m^2 and velocity as:

$$\int \vec{F}.\vec{V}\, dV \qquad (Eq. 3-22)$$

3.10.2 Turbulence intensity

The turbulence intensity is an indicator of local mixing efficiency and is calculated in FLUENT as:

$$\text{TI} = \frac{\text{RMS of the turbulet velocity fluctuations}}{\text{Mean velocity}} \qquad (Eq. 3-23)$$

3.10.3 Mixing efficiency

The trace scalar is used to detect global mixing efficiency. The standard deviation of UDS was calculated as:

$$STDEV\ (UDS) = \sqrt{AVG(UDS^2) - (AVG(UDS))^2} \qquad (Eq.\ 3-24)$$

The average of UDS scalar ± STDEV of UDS was used to detect mixing efficiency. When STDEV of UDS decreases to zero indicates to homogenization of scalar in the melt.

3.11 Heat transfer coefficient

The melting equation was used which is the heat balance at the interface of the melt and scrap which is written in one dimension as:

$$h(T_L - T_m) = \rho L r_m - k\frac{\partial T}{\partial x} \qquad (Eq.\ 3-25)$$

where T_L is melt temperature, T_m is melting temperature, k is thermal conductivity, and r_m is melting rate.

It was assumed that the interface temperature has increased to the melt temperature.

Melting rate, r_m, was calculated as:

$$r_m = \frac{1}{A}\frac{\Delta V}{\Delta t} \qquad (Eq.\ 3-26)$$

where A is the interface area, Δt is time step which was 0.25 s, and ΔV is volume changes of solid. It was assumed that the interface area is constant during melting since monitoring of interface area in each time step was expensive. Also, the heat conduction inside the scrap was neglected since as it will be shown the convective heat transfer is dominant using electromagnetic stirring, so Eq. 3-25 was simplified to:

$$h(T_L - T_m) = \rho L r_m \qquad (Eq.\ 3-27)$$

Heat transfer coefficient was calculated from Eq. 3-27 for all cases.

Then the Nusselt number was calculated using heat transfer coefficient.

3.12 Solid remaining

Volume decrease of solid during melting was expressed as the parameter, solid remaining:

$$Solid\ Remaining = \frac{Scrap\ volume_{(t)}}{Scrap\ volume_{(t=0)}} \qquad (Eq.\ 3-28)$$

To calculate heat transfer coefficient the time to reach 0.4 solid remaining, $t_{0.4}$, has been used.

Chapter 4

RESULTS AND DISCUSSION

4.1 Comparison between electromagnetic stirring and natural convection

Figure 4-1 shows velocity distribution for both cases with and without electromagnetic stirring in two cross sections through the center of the furnace in x and y directions after 400 seconds when melting has been finished. For the case natural convection, Figure 4-1 (a), the flow starts from the arcs having higher temperature towards the lateral walls with lower temperature, and then goes up towards the surface as two circulation loops can be recognized. It can be seen that velocity vectors with maximum magnitudes are concentrated only close to the surface, which can reach to 0.17 m/s, and the remained region, having the velocity lower than 0.08, is almost stagnant. It shows that natural convection has a negligible effect on velocity filed. This flow pattern is in good agreement with studies done by Szekely [4] and Gonzalez [6]. It should be mentioned that in real furnace, other factors such as oxygen lancing and alloying contribute to more circulation in the bath.

In contrast, when forward electromagnetic stirring is applied, Figure 4-1 (b), the flow has almost covered the entire bath. It can be seen that, in the EBT region, the velocity magnitude is lower, but, in comparison to natural convection, it has still higher value. The maximum velocity is about 1.21 m/s.

Figure 4-2 shows volume averaged velocity versus time for backward and forward stirring and natural convection. It can be seen that applying electromagnetic stirring, first, melt is accelerated which takes less than 300 s. for forward stirring after 300 s there is a stable velocity fluctuations around 0.5 m/s , while, for backward stirring, there are instabilities and the velocity magnitude is lower than forward stirring. For natural convection, the averaged velocity is close to zero.

Figure 4-3 shows temperature distribution for both cases after 400 s. For case natural convection, Figure 4-3 (a), a strong stratification occurs in the melt as three regions can be recognized: first the region close to the surface with the highest temperature, 2270 – 2500 K, second the middle region, temperature is about 1820 – 2270 K, and finally the region which covers most of the bath with temperature

between 1750 – 1820 K, which is almost stagnant. In contrast, when forward electromagnetic is applied, Figure 4-3 (b), temperature is almost homogenized, about 1830-1870 K, and stratification is eliminated.

As explained in section 2.10.1, the stirring power as a performance indicator was calculated using dissipation rate of mechanical energy for both cases with and without electromagnetic stirring. Figure 4-4 shows that applying electromagnetic stirring, after melt acceleration, the stirring power fluctuates around 1500 W, while for natural convection, stirring power is almost zero.

With electromagnetic stirring, stirring power was also calculated using mechanical power input rate. As illustrated in Figure 4-5, the stirring power calculated by mechanical power input rate is higher than the one calculated by dissipation rate of mechanical energy, about 200 W, and when the power input rate has maximum value, the dissipation rate of energy reaches to its minimum. The lower value of stirring power calculated by dissipation rate of energy can be due to the numerical diffusion which is a false diffusion and is popular in complex and convection dominated flows.

Turbulence intensity distribution, as explained in section 3.10.2, for both cases has been shown in Figure 3-6. With natural convection, the maximum turbulence intensity occurs close to the arc spots, which is about 6 %, and it is almost zero in the remained region, but, with electromagnetic stirring, the maximum value is about 26 %. Figure 4-7 shows the volume averaged turbulence intensity and velocity versus time. With electromagnetic stirring, the average turbulence intensity fluctuates around 12 % after melt acceleration, which is in positive correlation with melt velocity.

Mixing efficiency for both cases with and without electromagnetic stirring was calculated as explained in section 2.10.3. Figure 4-8 shows time versus average UDS ± STDEV. Applying electromagnetic stirring, after 100 s, standard deviation is almost zero, indicating that the scalar is homogenized, whereas, with natural convection, the values for average UDS ± STDEV have not converged to the average UDS, which is almost 0.6544, indicating the poor mixing in the bath.

4.2 Scrap melting

4.2.1 Effect of stirring

The vertical surface through the center of scrap was considered as illustrated in Figure 4-9. Figure 4-10 shows the velocity distribution in the bath for both cases with and without electromagnetic stirring after 60 s. For natural convection, Figure 4-10 (a), the flow descends from the hot surface towards lateral walls with lower temperature, and then, on the right side, it flows towards scrap, having the lowest

temperature in the melt, 300 K, and then it ascends from bottom towards the surface. The region at the bottom, on the right side, has almost high velocity magnitude, but still most region of the melt is stagnant. With electromagnetic stirring, Figure 3-8 (b), the flow covers almost the entire bath as more than sixty percent of the scrap has been disappeared.

Figure 4-11 shows temperature distribution for both cases. With only natural convection, strong stratification occurs, whereas using electromagnetic stirring, temperature is homogenized, and the superheated region close to the arc spots has been disappeared.

Figure 4-12 shows the solid region in the melt after 60 s. With natural convection, the solidified region covers the bottom surface around the scrap, and melting has not started, whereas with electromagnetic stirring more than sixty percent of the scrap has been melted. The solidified shell forming around the scrap has been shown in Figure 4-13. Solid remaining, as described in, versus time has been shown for both cases in Figure 4-14. It shows that, with natural convection, during the first seconds of melting, the amount of solid remaining increases and then decreases indicating the formation and remelting of the solidified shell which is formed around the scrap, the region above solid remaining =1, but it has been almost eliminated with electromagnetic stirring. It also shows that the melting time has been decreased significantly with electromagnetic stirring.

Figure 4-15 shows the minimum temperature versus time for both cases. The end time for both is the time to reach 0.2 solid remaining. It shows, with natural convection, the minimum temperature of scrap has increased to about 420 K, whereas it is unchanged with electromagnetic stirring. It shows the strong convective heat transfer in the bath using electromagnetic stirring and the conduction dominated melting with natural convection.

4.2.2 Effect of scrap size

Figure 4-16 shows that the amount of solid remaining for the scrap with R=0.1 m is maximum due to the smaller interface area between solid and melt, and it has also the lower melting time. Considering time after melting the solidified shell to time to reach 0.4 solid remaining, t_{40}, volume changes versus time were depicted, Figure 4-17, for three different scrap sizes, and linear lines were fitted, the slope of which can indicate to melting rate. It is shown that melting rate, m^3/s, for the scrap with R=0.2 m is maximum, 0.0003, which is due to the larger interface area. The correlation between melting time and scrap size is also shown in Figure 4-18.

4.2.3 Effect of stirring direction: Forward and backward

Temperature distribution for cases 1-8 after 60 s has been shown in Figure 4-19 and 4-20. In both backward and forward stirring, the higher force magnitude

contributes to better temperature homogenization, as applying the maximum force the superheated zone around the arc spots is almost disappeared. It can also be seen that, for the certain time, the amount of scrap decreases when force magnitude increases.

Figure 4-21 shows velocity distribution for case 8, backward stirring and FORCEMAG=1. Comparison between forward, Figure 3-10, and backward stirring shows applying forward force leads to better temperature homogenization and melting rate. In forward stirring, velocity direction is towards the scrap, whereas, in forward stirring, is vice versa, so it can be said that position of scrap in the melt is a determining factor in melting rate. In Figure 4-21, the velocity around the scrap changes almost between 0.16 and 0.22 m^3/s, while, in Figure 4-10, it changes between 0.19 and 0.26 m^3/s. The maximum velocity, in the whole melt, also, in forward stirring, is higher than backward stirring which was shown in Figure 4-2. It should be mentioned that the higher concentration of arrows around the scrap is due to grid refinement, and the velocity has been shown only in one surface and it is instantaneous velocity not mean velocity. Figure 4-22, solid remaining versus time for both forward and backward stirring, shows the melting time is lower with forward stirring, and during the first 10 s formation and melting of the solidified shell around the scrap occurs in backward stirring.

Figure 4-23 and 4-24 show the volume averaged velocity versus time for forward and backward stirring using different force magnitudes. It shows the melt velocity decreases by decrease of the force magnitude.

4.2.4 Effect of preheating

Figure 4-25 shows the effect of preheating on melting time. It shows the melting time decrease with initial temperature of scrap. Figure 4-26 shows the initial temperature of scrap versus melting time.

4.2.5 Heat transfer coefficient

The heat transfer coefficient, calculated as explained in 3.11, versus time has been shown for all cases in Figure 4-27, 4-28 and 4-29. The end time is the time to reach 0.4 solid remaining in the melt. With natural convection, Figure 4-27, the heat transfer coefficient ranges between 400-1200 W/m^2K. Figure 4-28 and 4-29, show the heat transfer coefficient increases when the force magnitude increases as it can reach to 50000 W/m^2K when FORCEMAG=1. They also show that with forward stirring the heat transfer coefficient has higher value.

Heat transfer coefficient is a function of factors such as melt properties, temperature and shape of the interface between melt and solid and the velocity of the melt. For natural convection where melt velocity is close to zero, so the melting rate is low, the heat transfer coefficient is lower and its changes continuously. For forward stirring velocity fluctuation is more stable than backward stirring, Figure 4-23 and 4-24, so the heat

transfer coefficient is also more stable. Heat transfer coefficient decreases since the interface area was considered unchanged, while it decreases during melting.

The average of heat transfer coefficient during the time to reach 0.4 solid remaining was calculated and the results versus different force magnitudes and time averaged velocity after 600, which is a constant value and independent of scrap size and temperature, have been shown in Figure 4-30 and 4-31 respectively. The results show that by increasing force magnitude, the melt velocity increases which contribute to higher heat transfer coefficient. The results achieved for heat transfer coefficient is in good agreement by values achieved by Gaye et al. [22].

The dimensionless Nusselt number was first calculated by the correlation suggested by Kerith, Eq. 2-23, and then it was calculated using heat transfer coefficient and Eq. 2-19. The Reynolds and Prandtl numbers were also calculated using Eq. 2-4 and Eq. 2-20 respectively. It was assumed that n in Eq. 2-21 is equal 0.805 the same as Kerith correlation, and then the amount of C was estimate. Figure 4-32 and 4-33 show the comparison between Nusselt number calculated by Kerith correlation and the one calculated by heat transfer coefficient for forward and backward stirring, and it also shows the difference between values of C. since decrease of interface area was not included, the calculations were done during the time to reach 0.7 solid remaining.

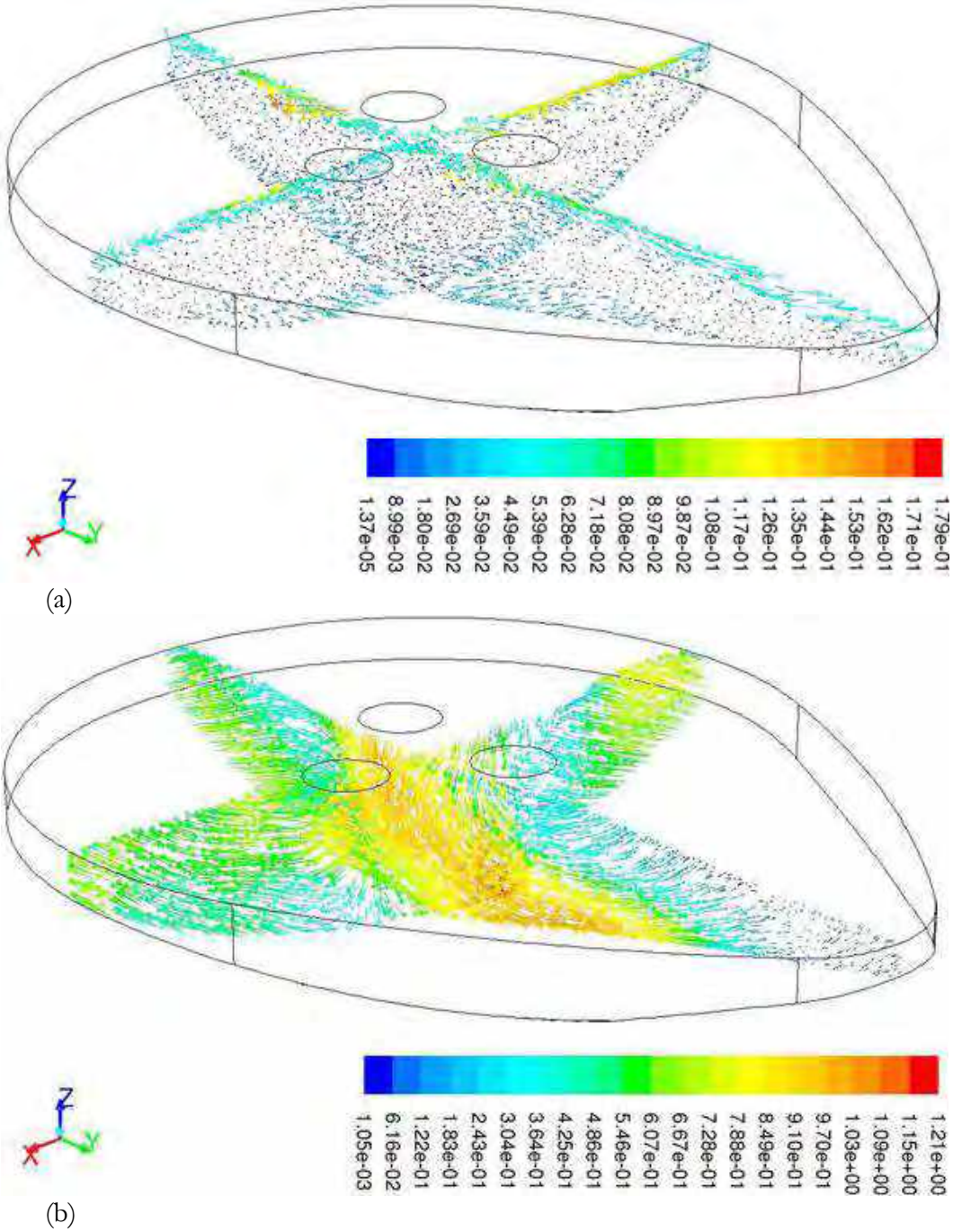

Figure 4-1. Comparison between velocity distribution of (a) natural convection (case 9) and (b) electromagnetic stirring (case 4); after 400 s.

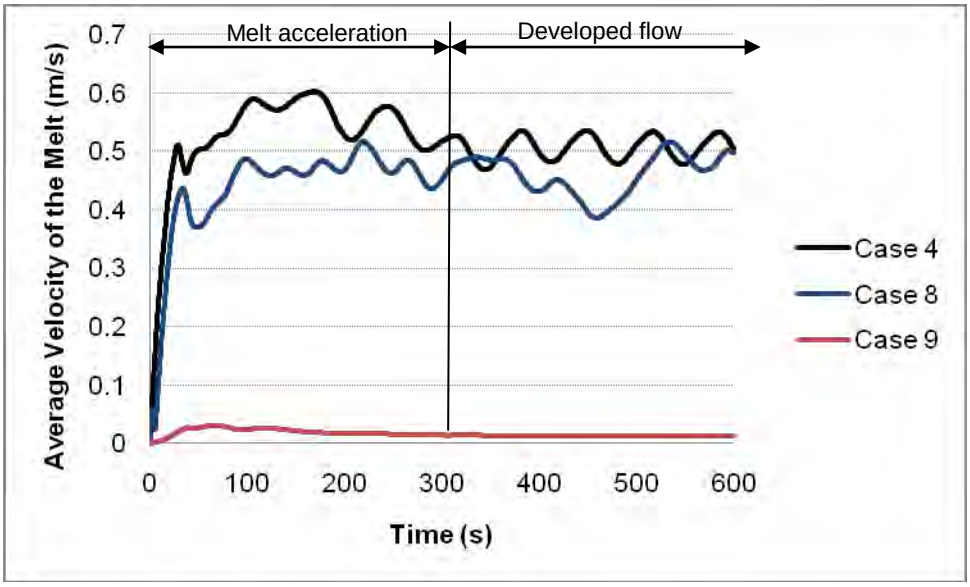

Figure 4- 2. Comparison between velocity of melt for natural convection (case 9) and backward (case 8) and forward (case 4) stirring.

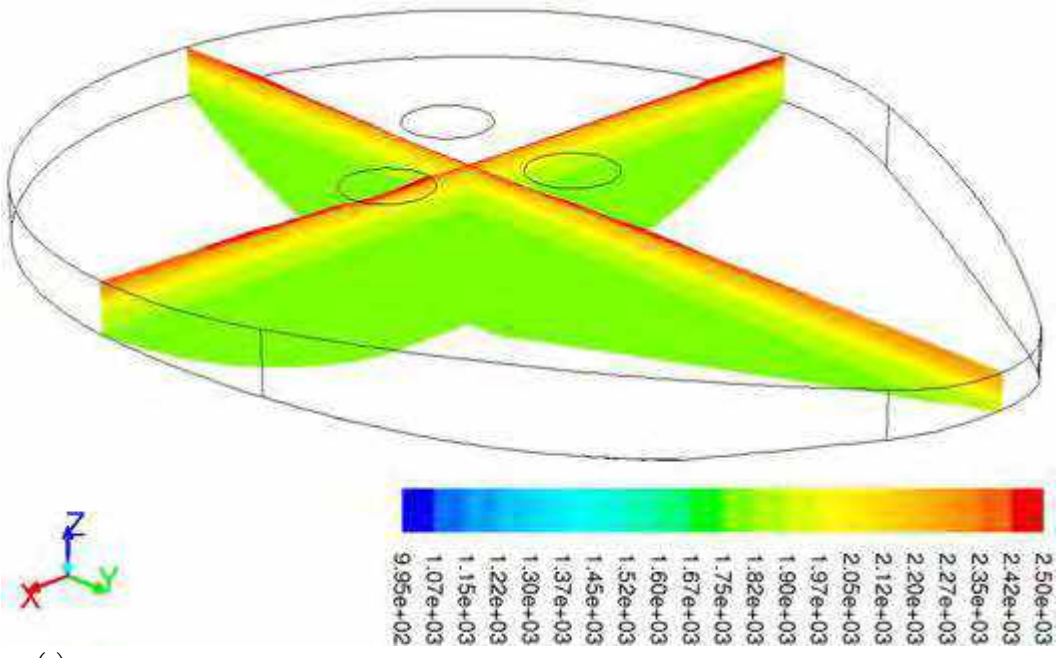

(a)

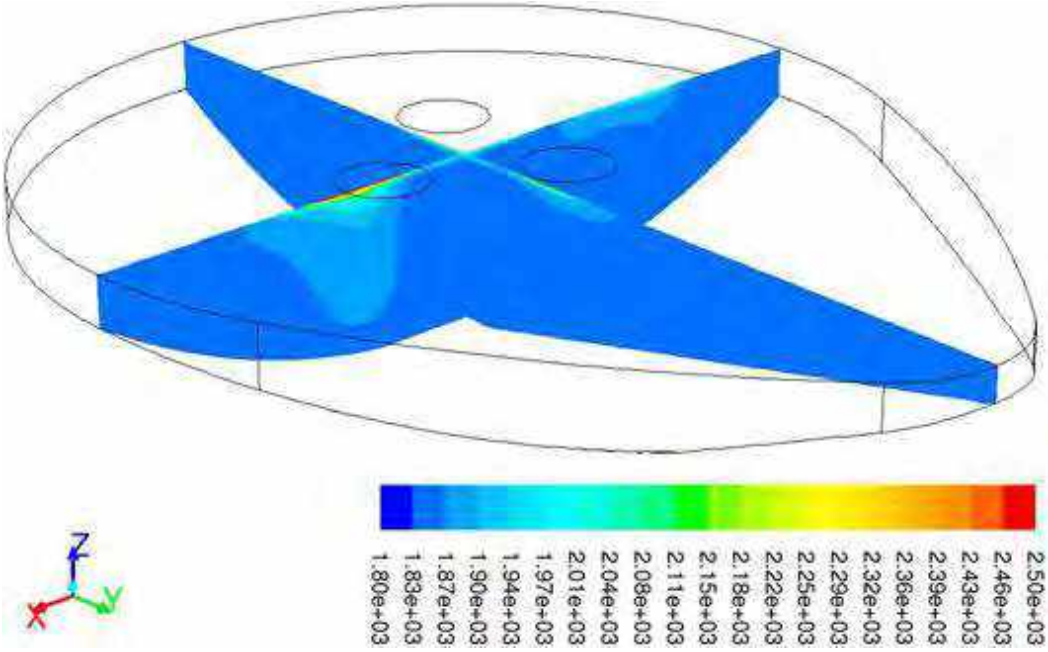

(b)

Figure 4-3. Comparison between temperature distribution of (a) natural convection (case 9) and (b) electromagnetic stirring (case 4); after 400 s.

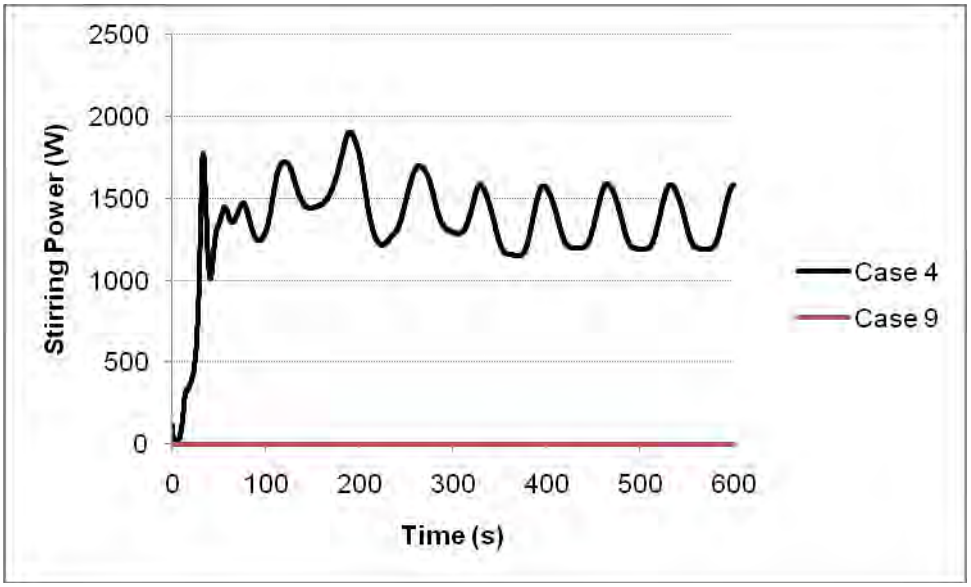

Figure 4-4. Comparison between stirring power, calculated by dissipation rate of mechanical energy, of electromagnetic stirring (case 4) and natural convection (case 9).

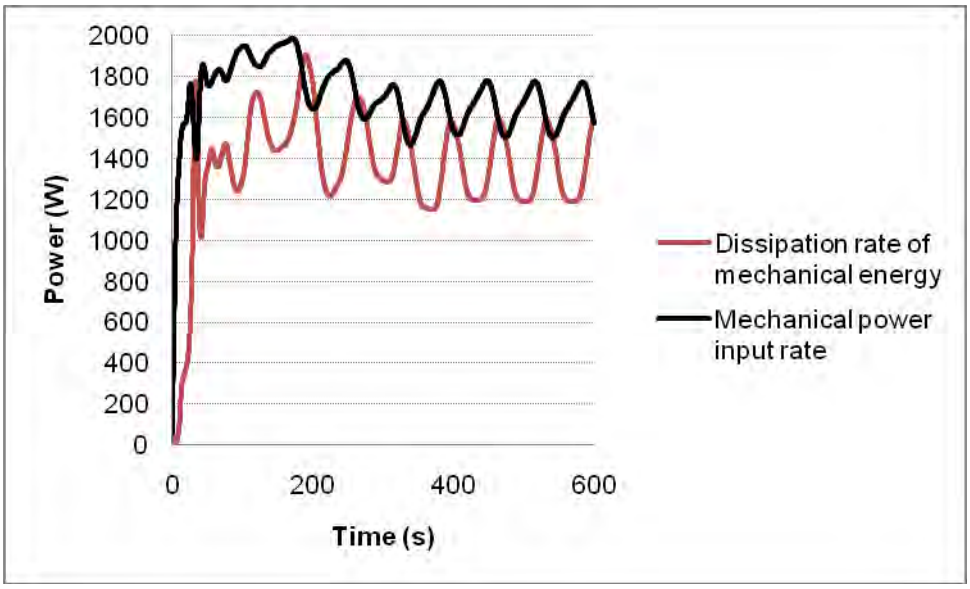

Figure 4-5. Comparison between stirring power calculated by dissipation rate of mechanical energy and mechanical power input rate; forward stirring and FORCEMAG=1.

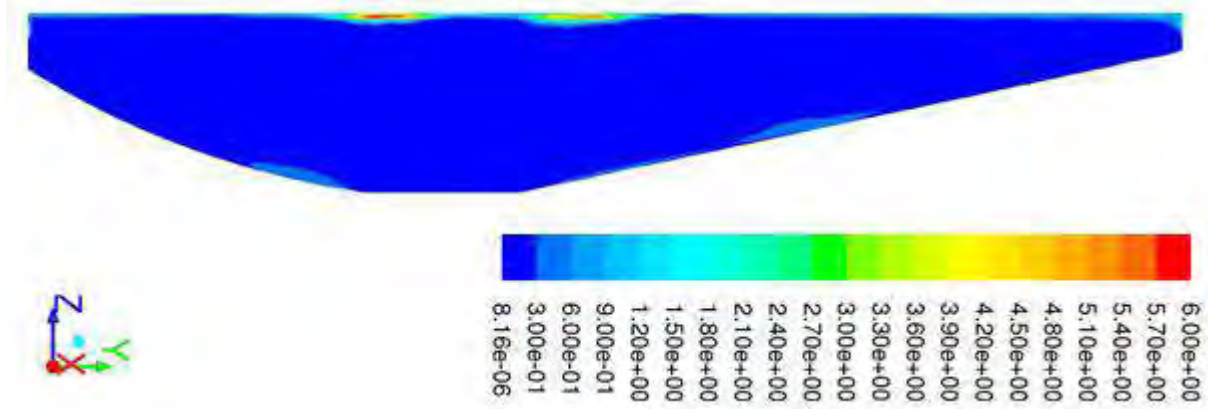

(a)

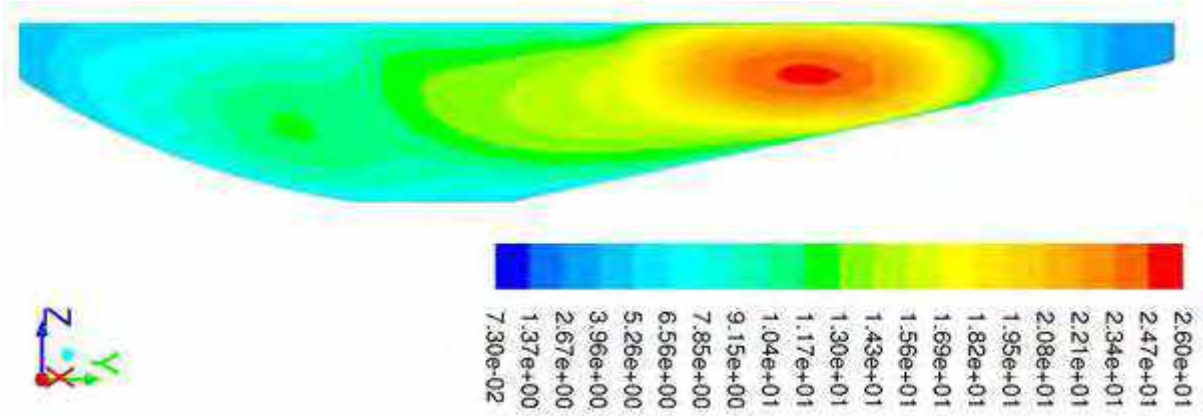

(b)

Figure 4-6. Comparison between turbulence intensity of (a) natural convection (case 9) and (b) electromagnetic stirring (case 4); after 400s.

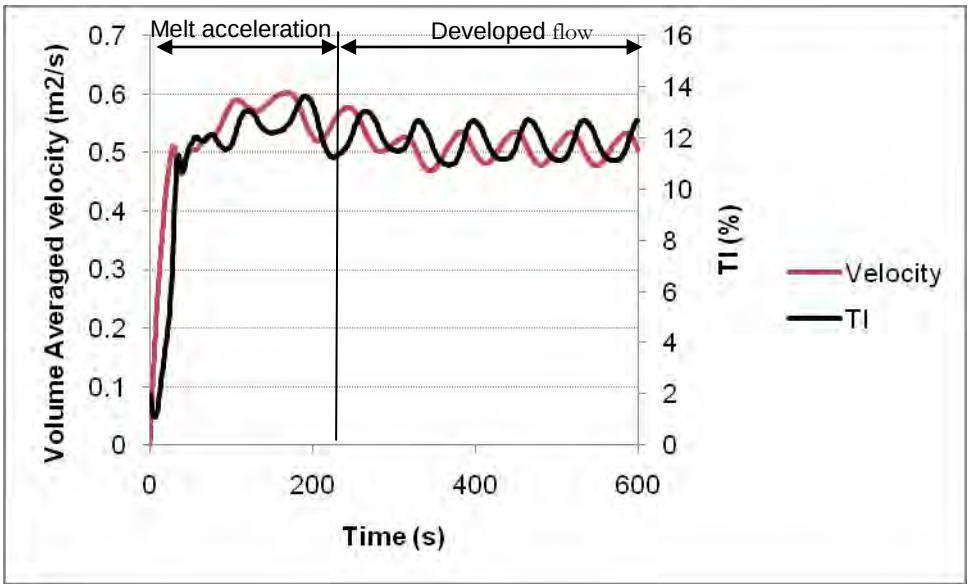

Figure 4- 7. Volume averaged velocity and turbulence intensity (TI) vs. time; forward stirring and FORCEMAG=1.

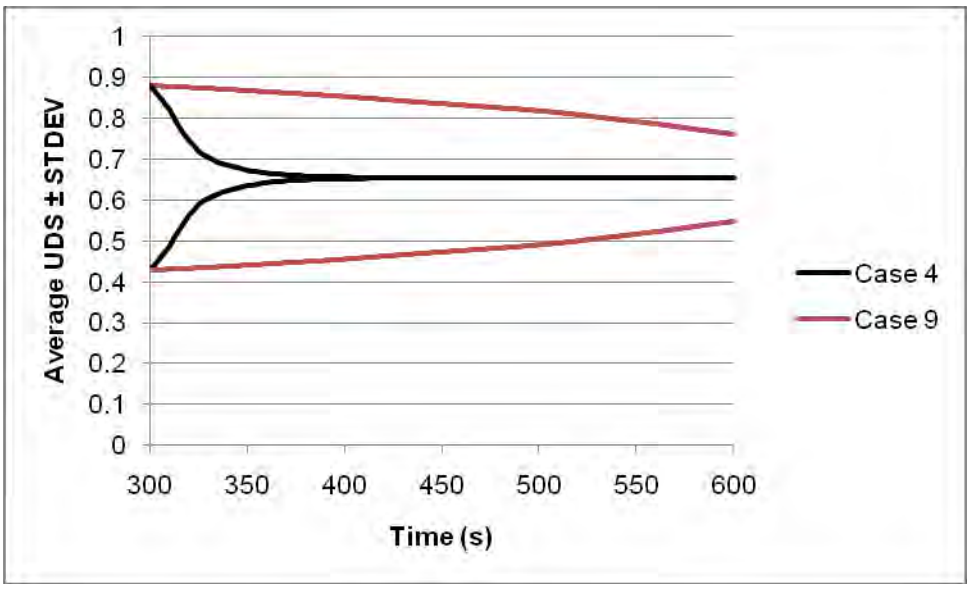

Figure 4-8. Comparison between mixing efficiency of electromagnetic stirring (case 4) and natural convection (case 9).

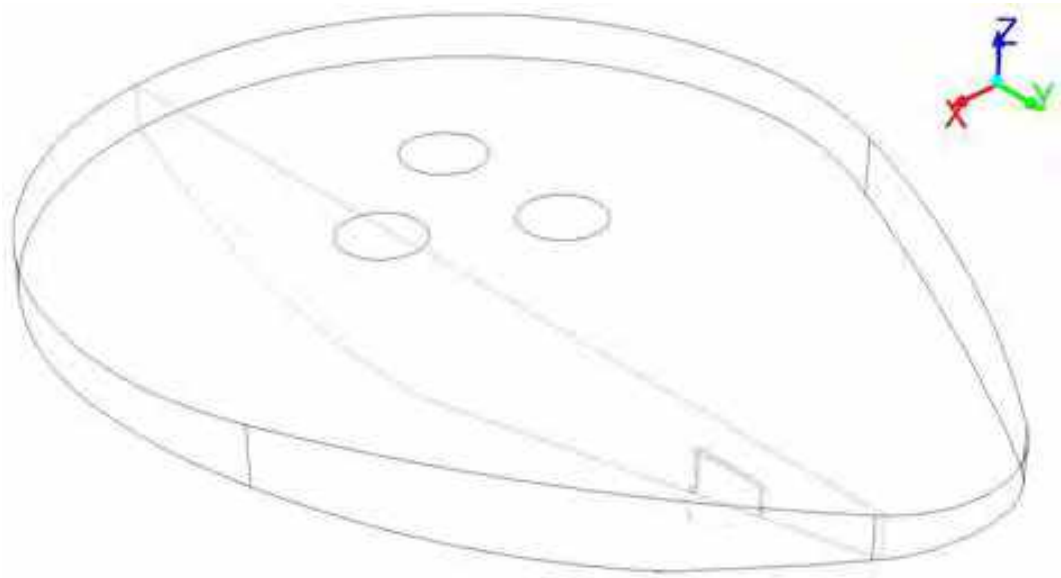

Figure 4-9. The middle section through the scrap in the melt.

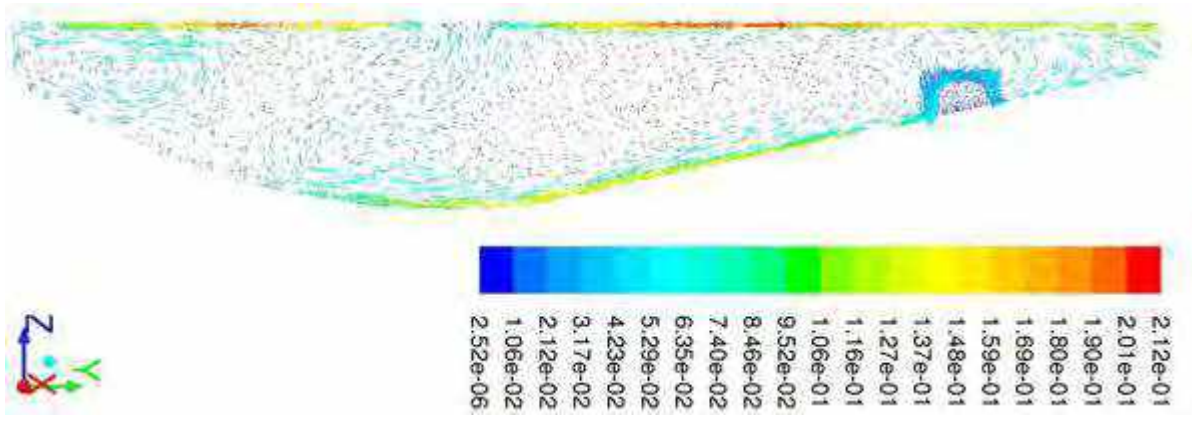

(a)

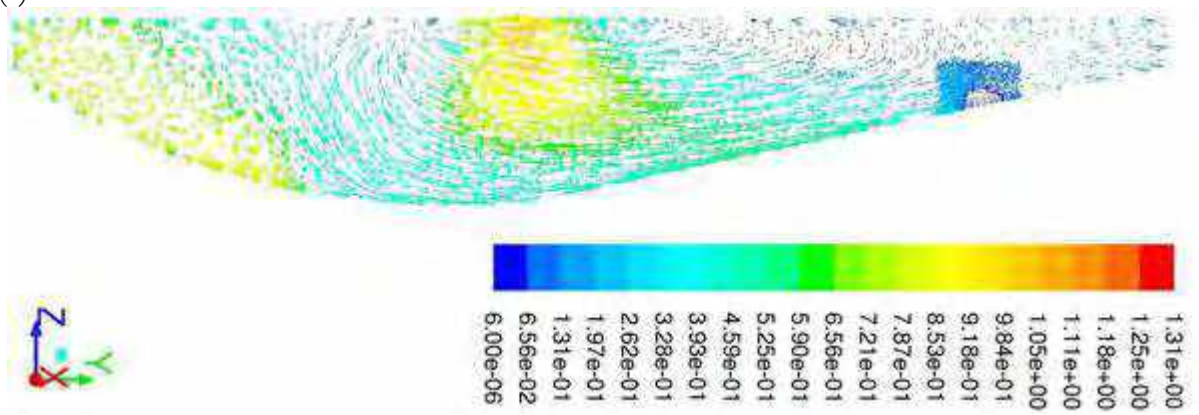

(b)

Figure 4-10. Comparison between velocity distribution of (a) natural convection (case 9) and (b) electromagnetic stirring (case 4); after 60 s.

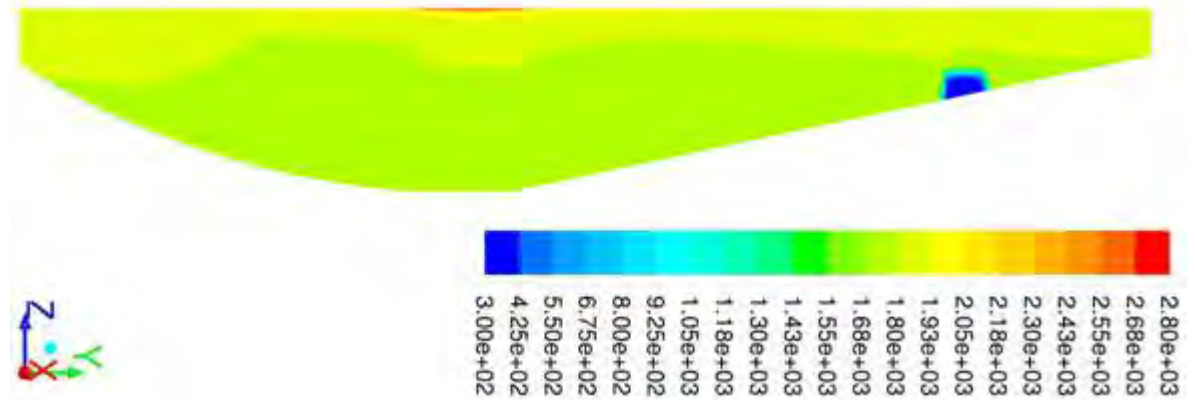

(a)

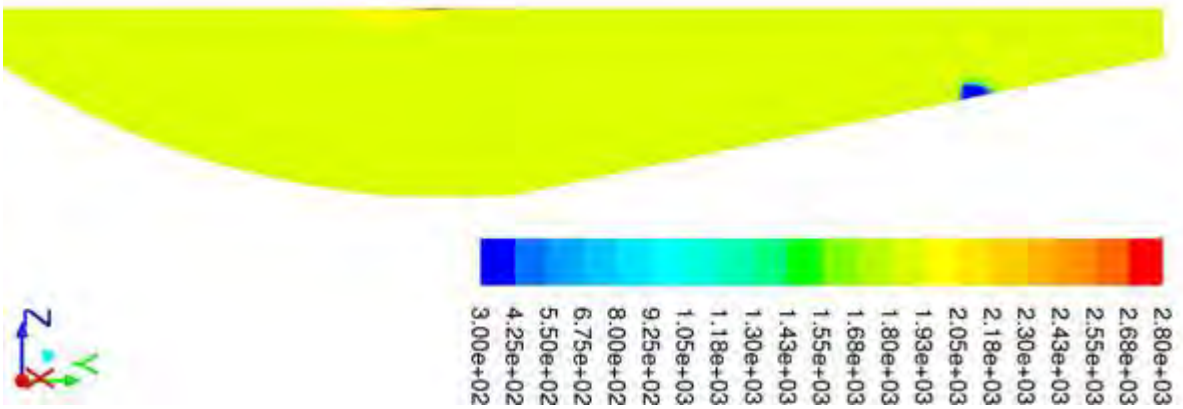

(b)

Figure 4-11. Comparison between temperature distribution of (a) natural convection (case 9) and (b) electromagnetic stirring (case 4); after 60 s.

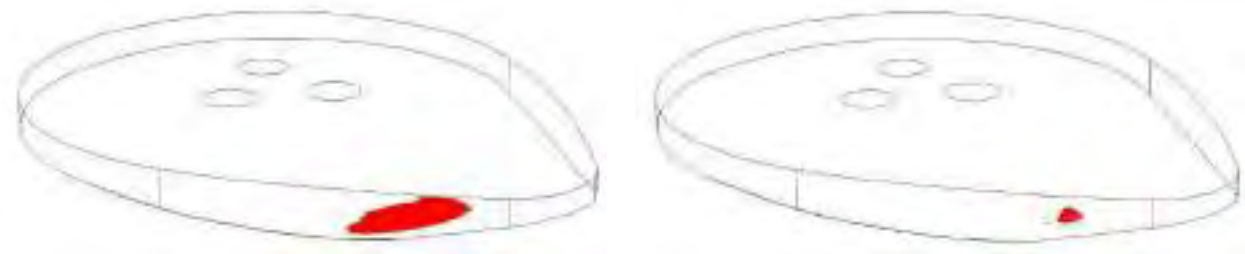

(a) (b)

Figure 4-12. The solid region in the melt for (a) natural convection (case 9) and (b) electromagnetic stirring (case 4); after 60 s.

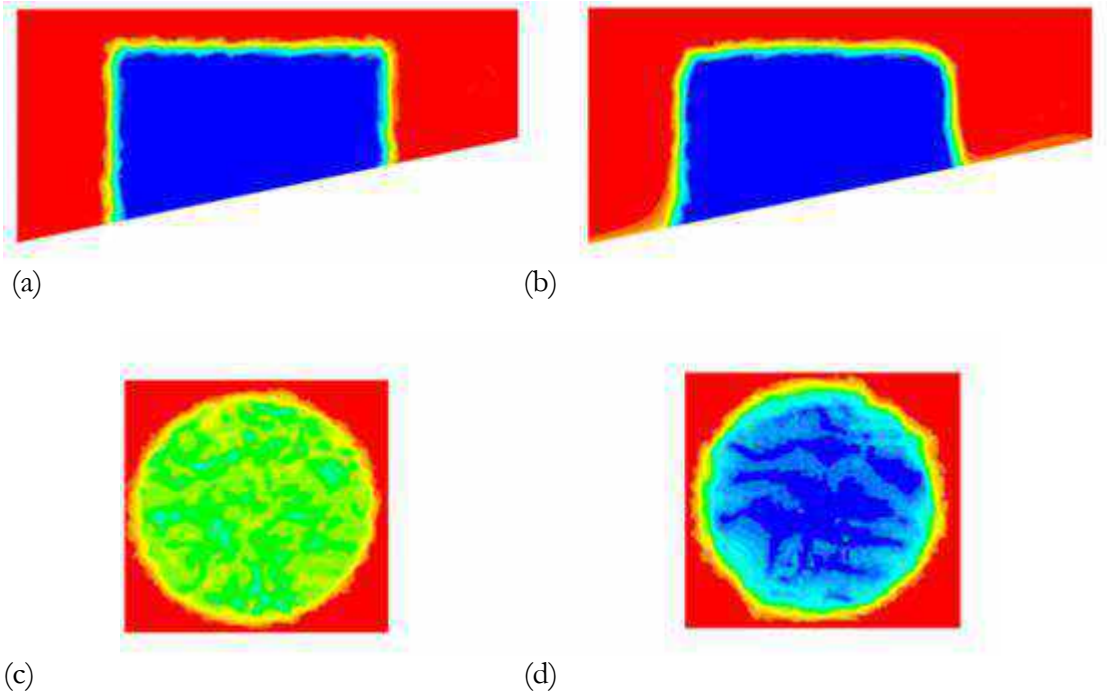

Figure 4-13. Formation of solidified shell around the scrap for natural convection (case 9) (a) and (c) cross sectional and top view of scrap for t=0, and (b) and (d) cross sectional and top view of scrap for t=18s.

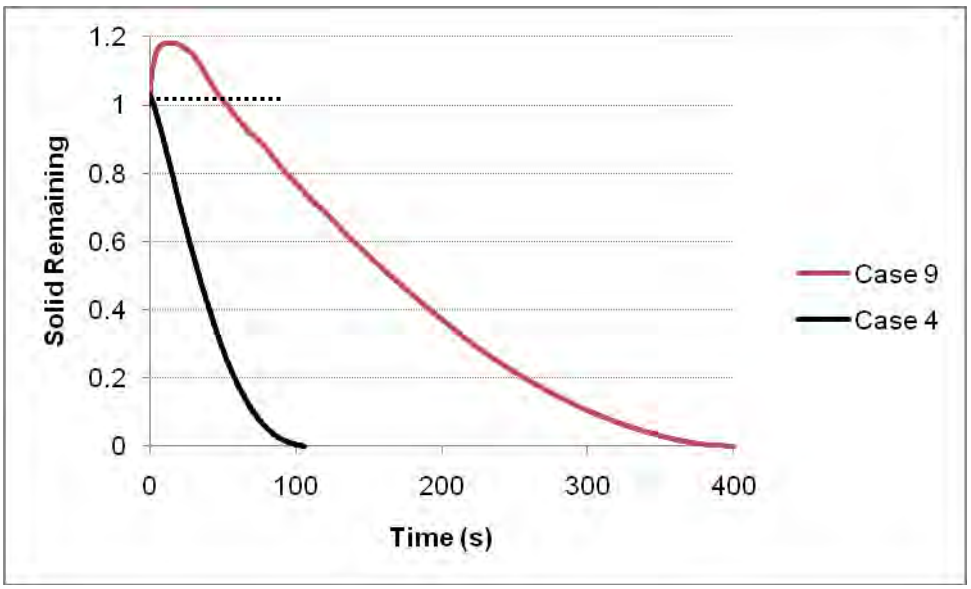

Figure 4-14. Comparison between melting of electromagnetic stirring (case 4) and natural convection (case 9).

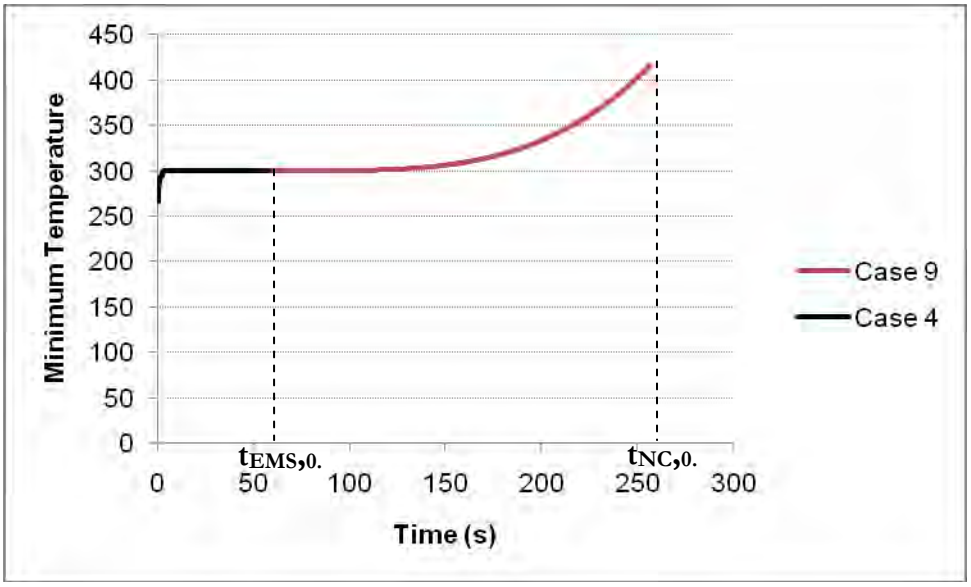

Figure 4-15. Comparison between minimum temperature of electromagnetic stirring (case 4), and natural convection (case 9) during the time to reach 0.2 solid remaining.

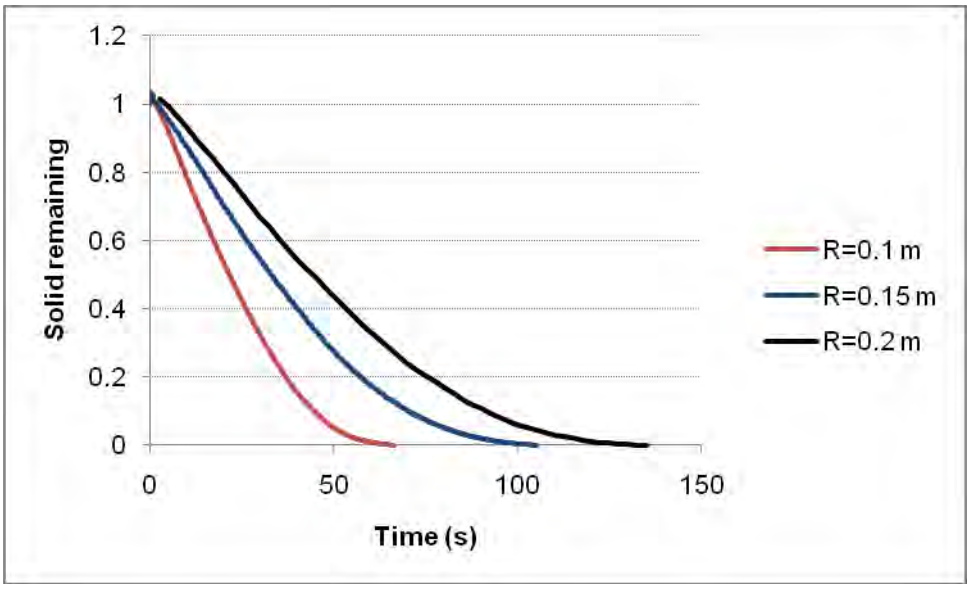

Figure 4-16. Comparison between melting time for 3 different radii

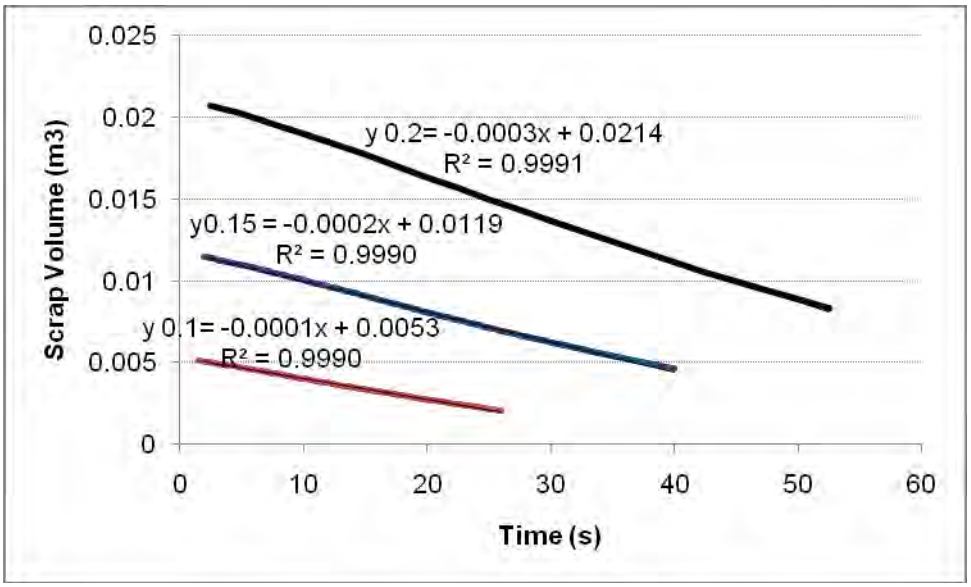

Figure 4-17. Comparison between melting rate of 3 different radii.

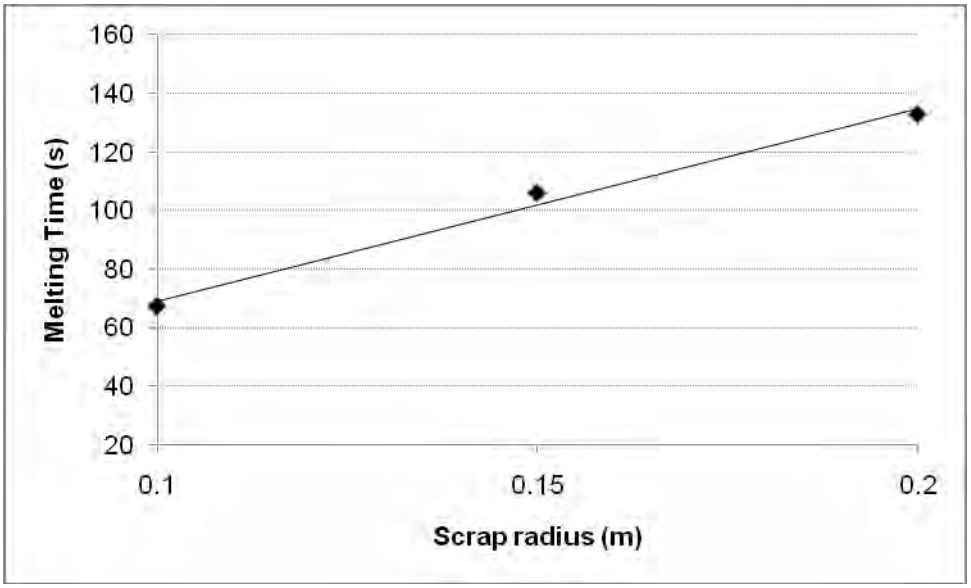

Figure 4-18. Melting time for 3 different scrap radii.

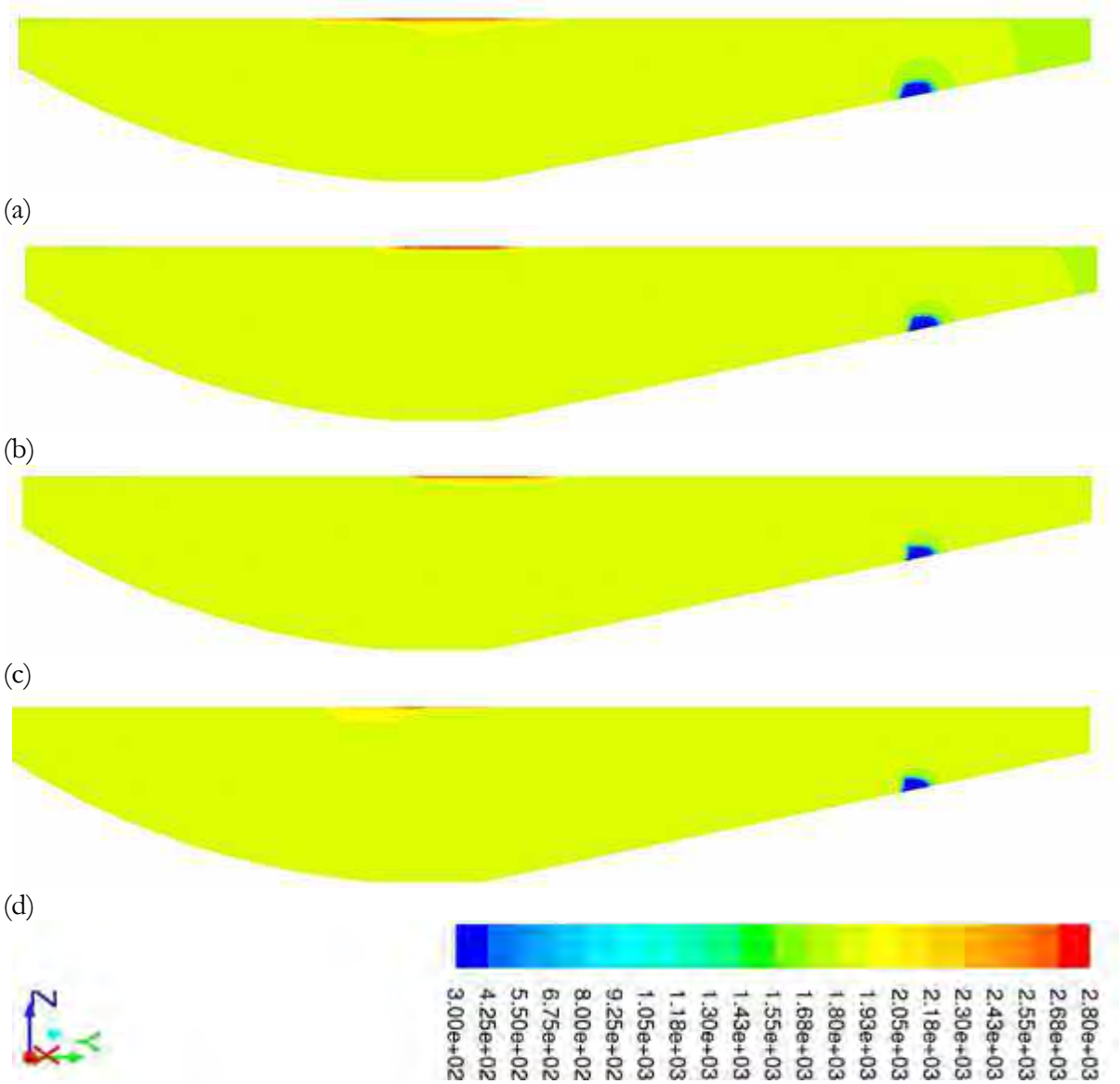

Figure 4-19. Temperature distribution for forward stirring for (a) FORCEMAG=0.25, (b) FORCEMAG=0.5, (c) FORCEMAG=0.75 and (d) FORCEMAG=1.

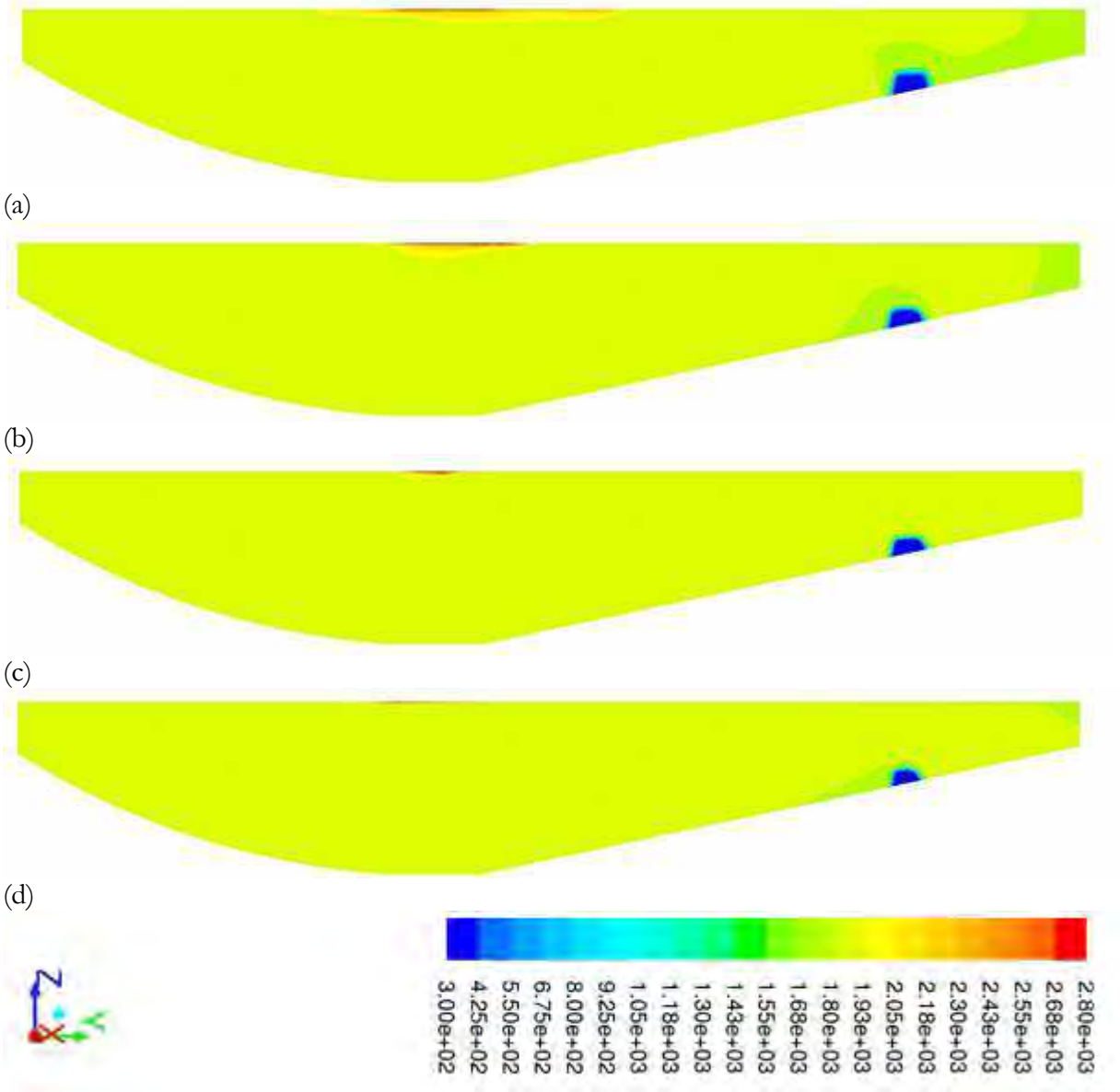

Figure 4-20. Temperature distribution for backward stirring for (a) FORCEMAG=0.25, (b) FORCEMAG=0.5, (c) FORCEMAG=0.75 and (d) FORCEMAG=1.

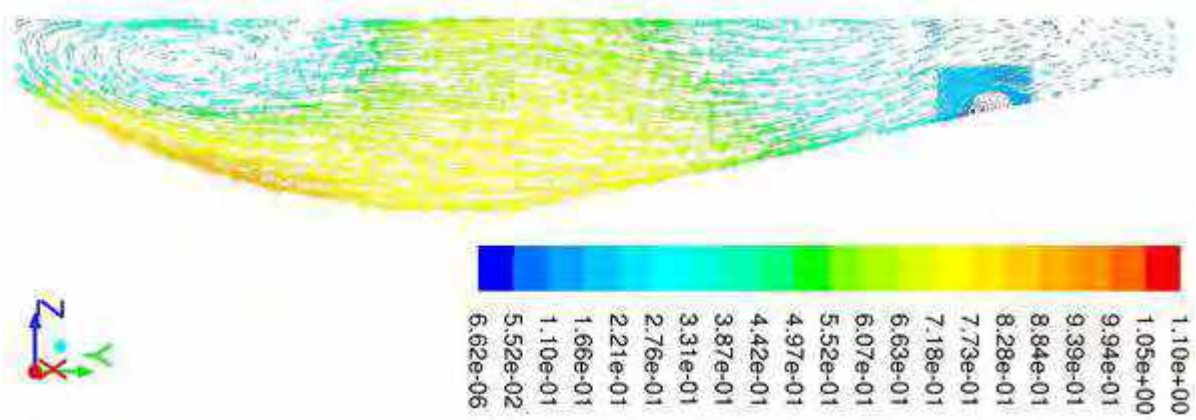

Figure 4-21. Velocity distribution for backward stirring (case 8); after 60 s.

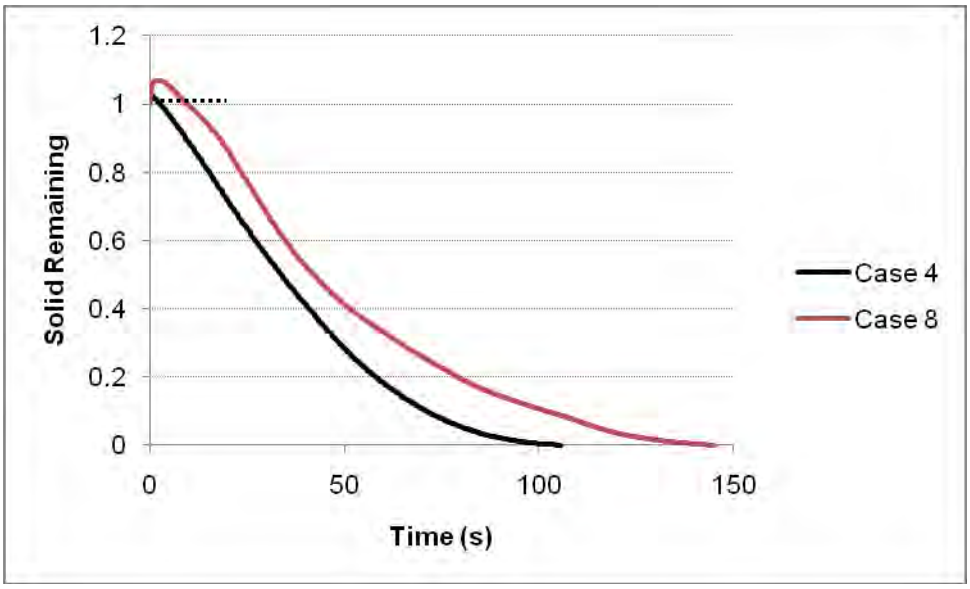

Figure 4-22. Comparison of solid remaining for backward (case 8) and forward stirring (case 4).

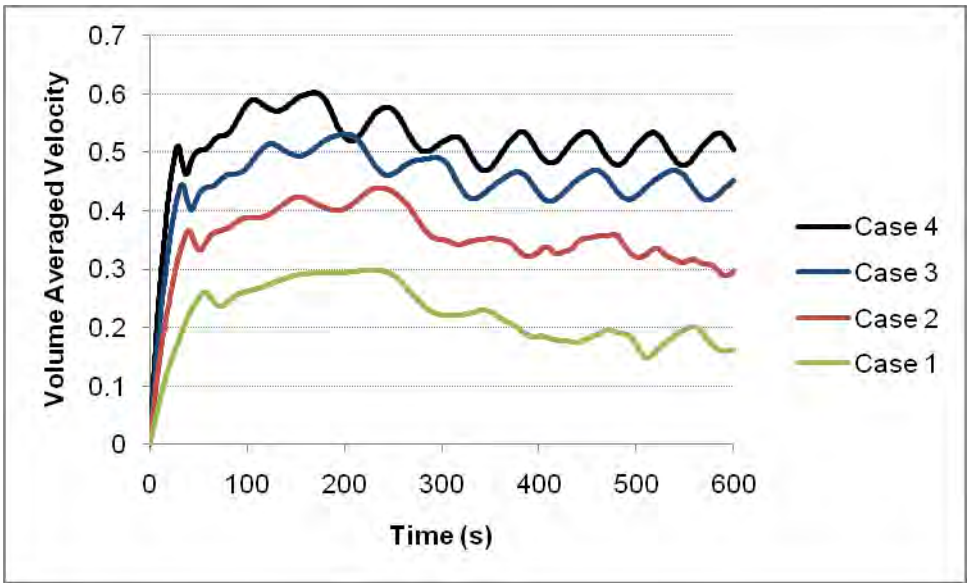

Figure 4-23. Volume averaged velocity vs. time; forward stirring and FORCEMAG=0.25, 0.5, 0.75 and 1 (case 1, 2, 3 and 4).

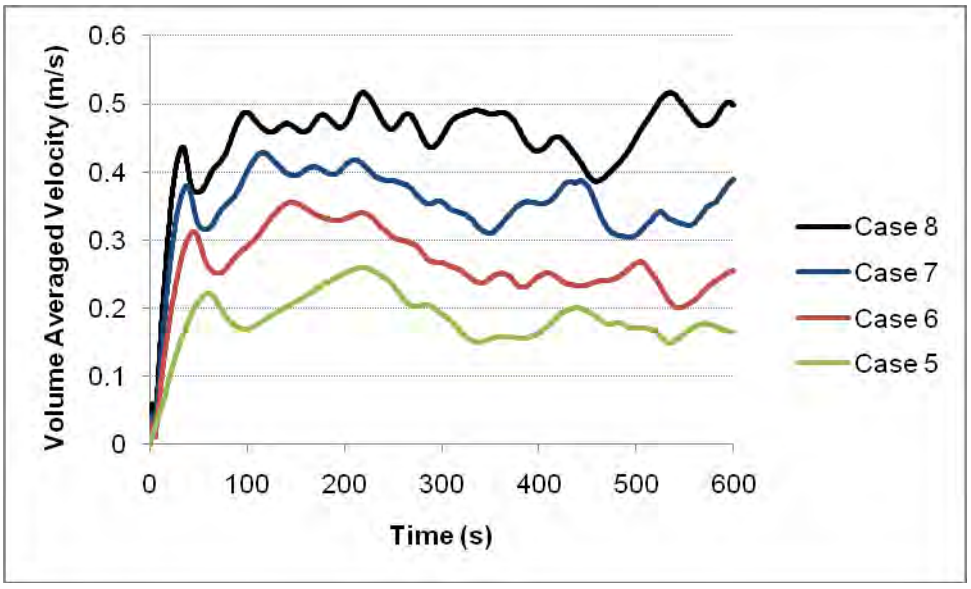

Figure 4-24 Volume averaged velocity vs. time; backward stirring and FORCEMAG=0.25, 0.5, 0.75 and 1 (case 5, 6, 7 and 8).

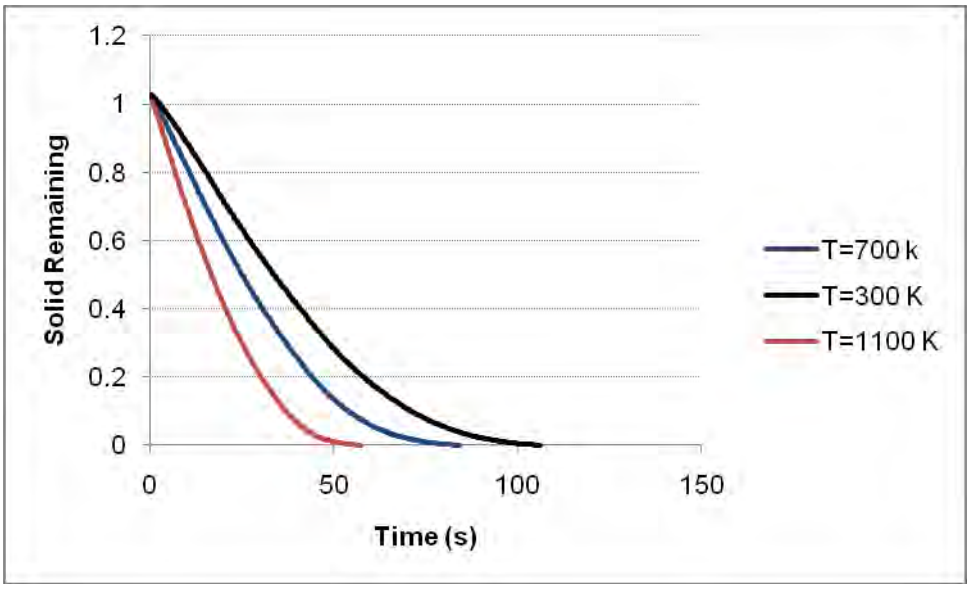

Figure 4-25. Comparison between melting for different initial scrap temperatures, 300, 700 and 1100 k.

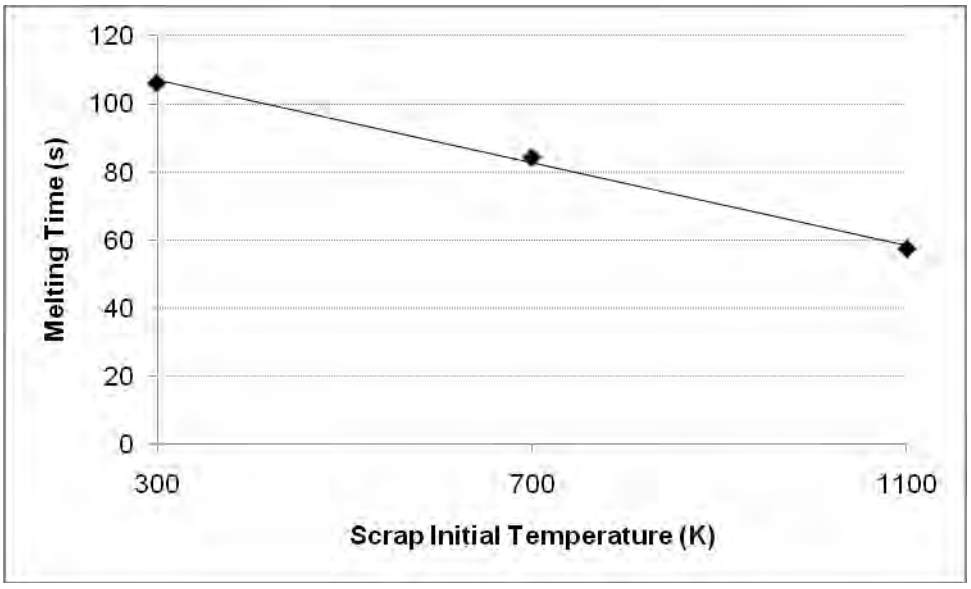

Figure 4-26. Melting time for 3 different initial scrap temperatures.

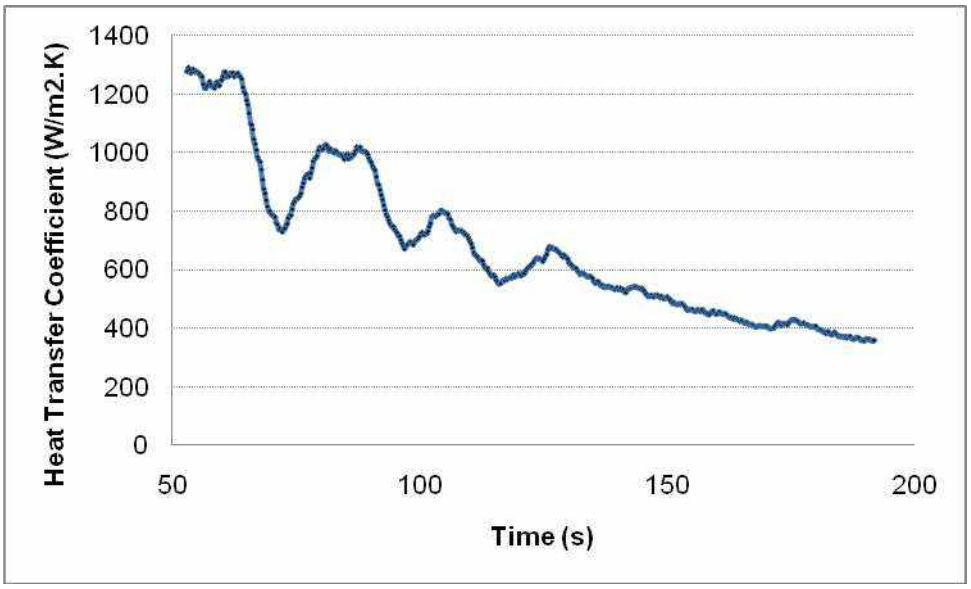

Figure 4-27. Heat transfer coefficient vs. time to reach 0.4 solid remaining for natural convection (case 9).

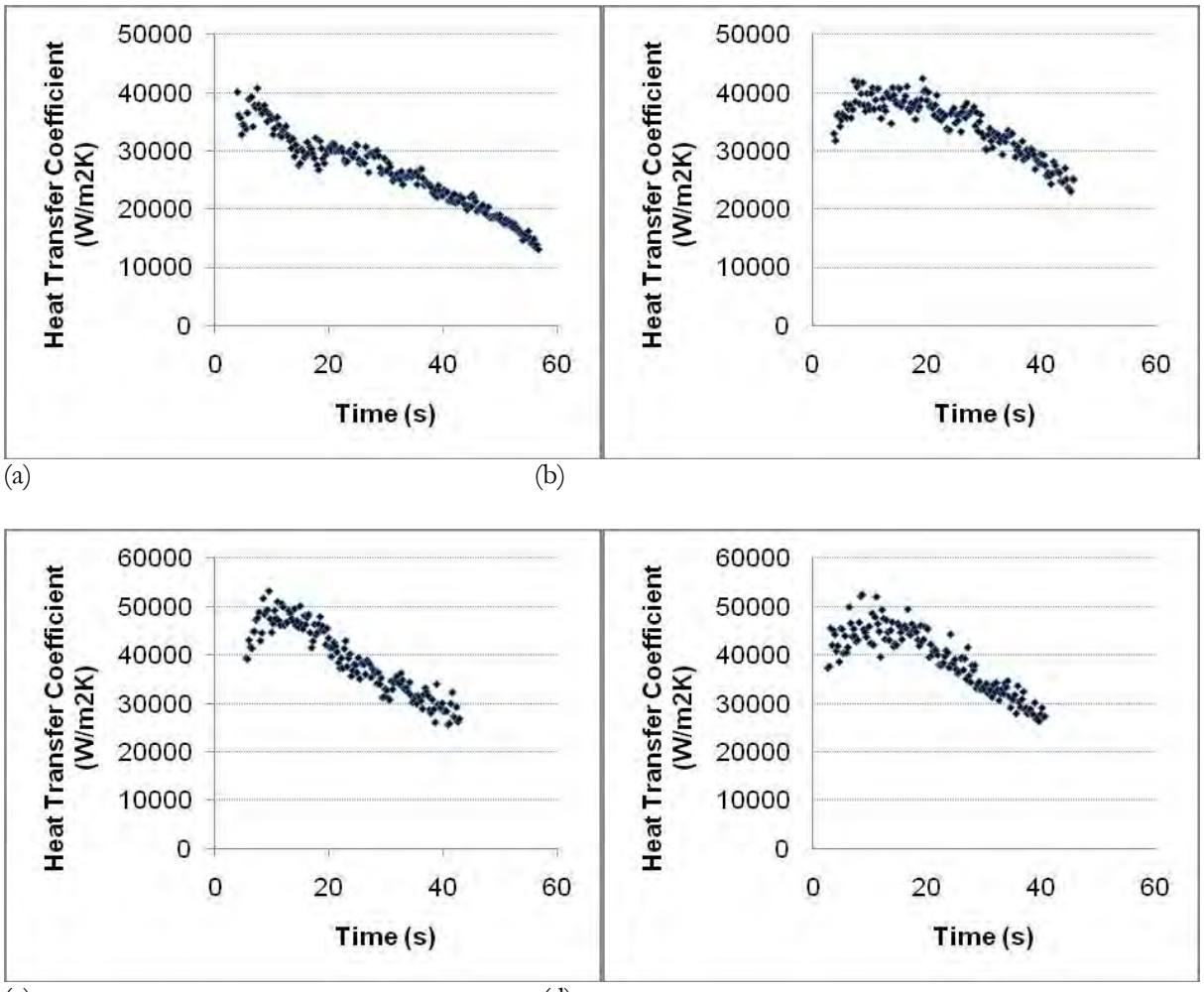

Figure 4-28. Heat transfer coefficient vs. time to reach 0.4 solid remaining for forward stirring (a) FORCEMAGe=0.25, (b) FORCEMAG=0.5, (c) FORCEMAG=0.75 and (d) FORCEMAG=1.

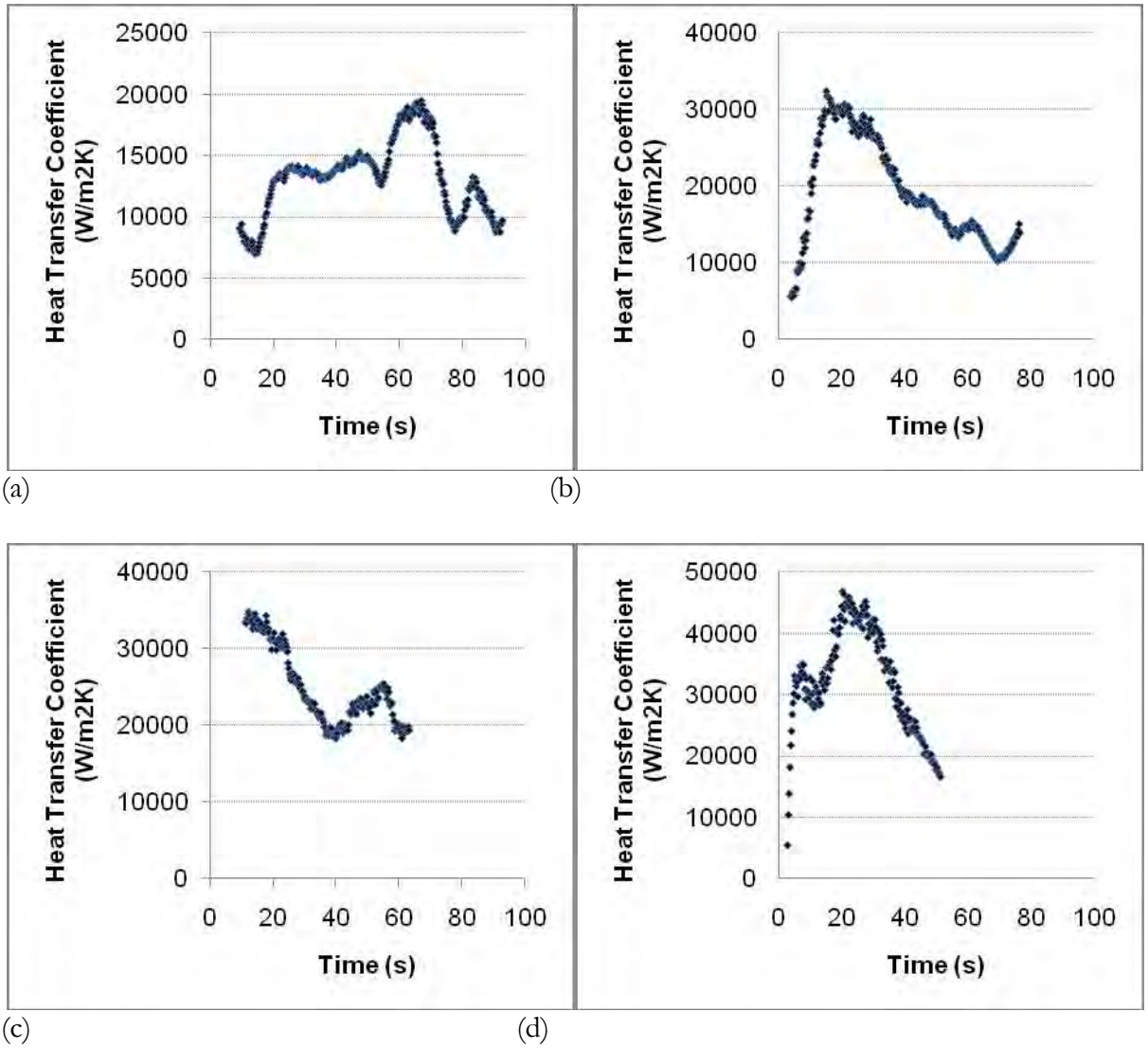

Figure 4-29. Heat transfer coefficient vs. time to reach 0.4 solid remaining for backward stirring (a) FORCEMAGe=0.25, (b) FORCEMAG=0.5, (c) FORCEMAG=0.75 and (d) FORCEMAG=1.

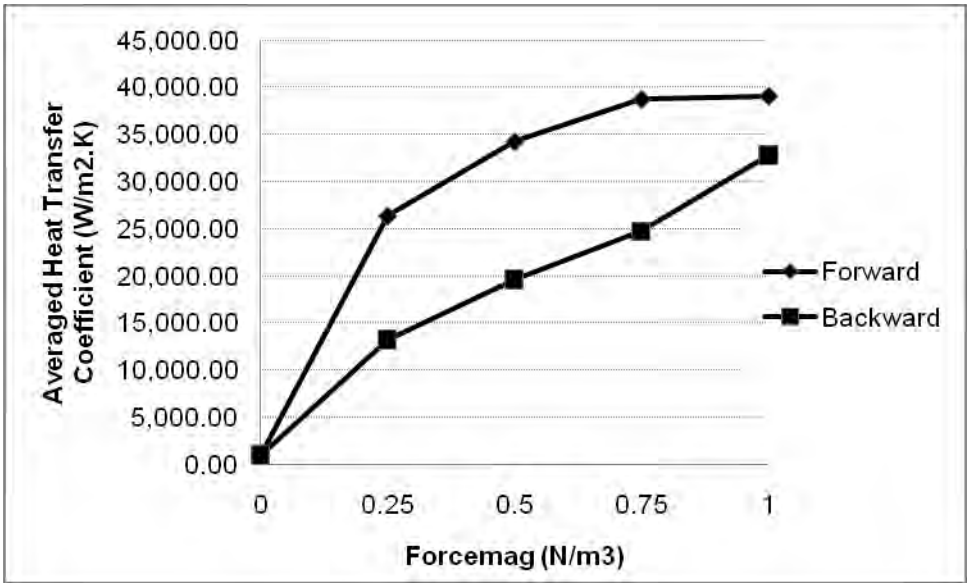

Figure 4-30. Averaged heat transfer coefficient vs. force magnitudes after 600s.

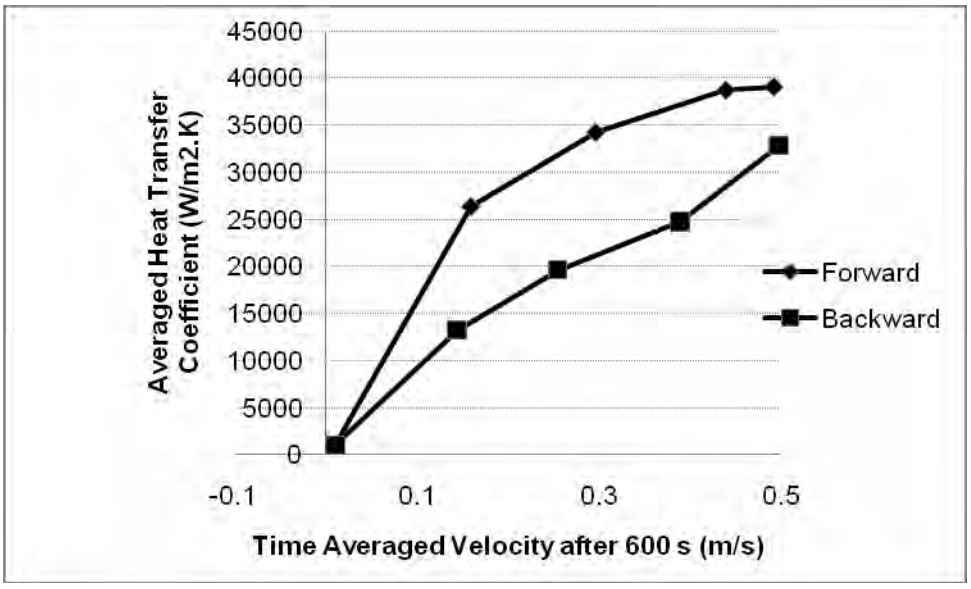

Figure 4-31. Averaged heat transfer coefficient vs. time averaged velocity after 600s for different force magnitudes.

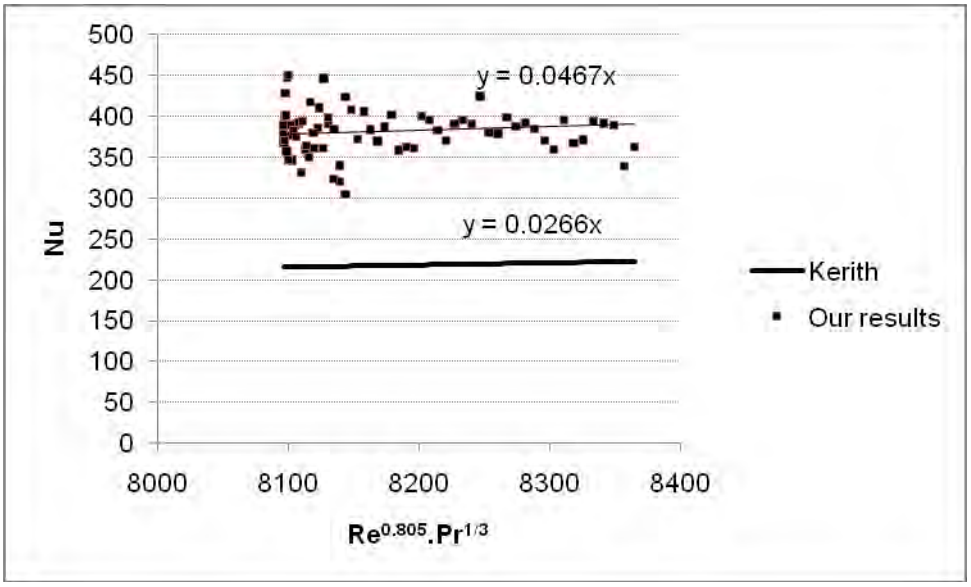

Figure 4-32. Nu number correlation calculated using Kerith results and our results; forward stirring and FORCEMAG=1; time to reach 0.7 solid remaining.

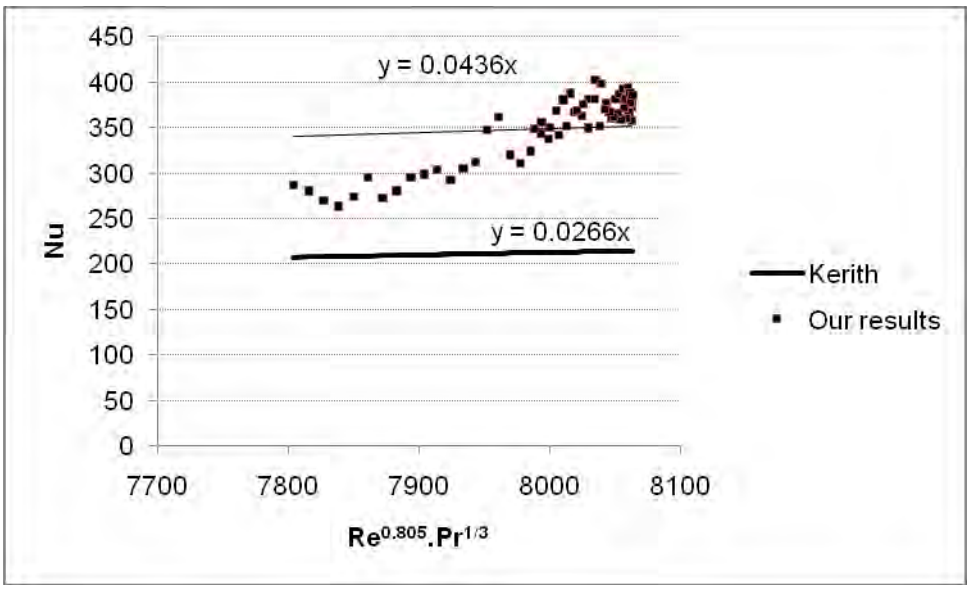

Figure 4-33. Nu number correlation calculated using Kerith results and our results; backward stirring and FORCEMAG=1; time to reach 0.7 solid remaining.

Chapter 5

CONCLUSION

Numerical modeling was used to study fluid flow, temperature distribution, mixing phenomena and heat transfer in an EBT EAF considering buoyancy and electromagnetic forces as driving forces separately.

It was observed using electromagnetic forces, velocity increases significantly and leads to a strong circulation which covers all the bath, so thermal stratification is almost eliminated and superheated zones close to the arc spots are removed and temperature is homogenous the entire bath.

Electromagnetic stirring also leads to an efficient mixing and reduced concentration gradients in the bath.

It was shown that the melting time is reduced by decreasing the size of scrap and increasing the initial temperature of scrap.

Computation of heat transfer coefficient showed using electromagnetic stirring the heat transfer coefficient can increase by a factor of 4, and electromagnetic stirring contributes to the higher melting rate and lower melting time which is due to the strong convective heat transfer in the bath.

Chapter 6

FUTURE WORKS

More than one scrap is used to model the real state of EAF, so interaction between the scraps such as formation of steel icebergs and porosity between the scraps can be investigated.

The three phase volume of fluid (VOF) model is used to include the slag layer and air above the melt to study how the slag layer flows on the melt surface.

REFERENCES

1. Schmitt R. J., *Introduction to electric arc furnace steelmaking*, EPRI Center for material production, 1985.

2. Jones J. A. T., *Electric arc furnace*, Steel Making and Refining Volume, Pittsburgh, 1998, 525 – 660.

3. Toulouevski Y. N. and Zinurov I. Y., *Innovation in electric arc furnaces*, Springer Heidelberg Dordrecht London New York, 2010.

4. Szekely J., McKelliget J. and Choudhary M, *Heat – transfer fluid flow and bath circulation in electric – arc furnaces and DC plasma furnaces*, Ironmaking and Steelmaking, 10(4), 1983, pp. 169-179

5. Kirschen M., Rahm C., Jeitler J. and Hackl G., *Steel flow characteristics in CFD improved EAF bottom tapping systems*, Vol. 23, 2008. Pp. 365 – 371.

6. Gonzalez O. J. P., Ramirez M. and Conejo A. N., *Effect of arc length on fluid flow and mixing phenomena in AC electric arc furnaces*, ISIJ International, Vol. 50, 2010, pp. 1 – 8

7. Sanchez J. L. G., RamÍrez-Argáez M. and Conejo A. N., *Power delivery from the arc in AC electric arc furnaces with different gas atmospheres*, Steel Research International, Vol 80, 2009, pp. 113 – 120.

8. Li J., Provatas N. and Irons G. A., Modeling of scrap melting in the heel of an EAF, AIST Transactions, Vol. 5, No. 3, 2008, pp. 216 – 223.

9. Li J., Brooks G. and Provatas N., Kinetics of scrap melting in liquid steel, Metallurgical and Materials Transaction B, 2005, pp. 293 – 302.

10. Li J. and Provatas N. Kinetics of scrap melting in liquid steel: multipiece scrap melting, Metallurgical and Materials Transactions B, Vol. 39, 2008, pp. 268 – 279.

11. Wu Y. K. and Lacroix M., *Numerical simulation of the melting of scrap metal in a circular furnace*, Int. Comm. Heat Mass Transfer, Vol. 22, No. 4, 1995, pp. 517 – 525.

12. Schmitt R., *Understanding electric arc furnace operations*, EPRI Center for Material Production,1987.

13. RamÍrez-Argáez M. A., Conejo A. N. and Guzmán Y. I. C., *Influence of the top slag layer on the flow dynamics in AC –electric arc furnaces*, International Journal Engineering Systems Modelling and Simulation, Vol. 2, No. 4, 2010, pp. 217 – 225.

14. David F., Tudorache T. and Firteanu V., *Numerical evaluation of electromagnetic field effects in electric arc furnaces*, COMPEL: The International Journal for Computation

and Mathematics in Electrical and Electronic Engineering, Vol. 20, 2001, pp. 619 – 635.

15. Wang F., Jin Z. and Zhu Z., *Fluid flow modeling of arc plasma and bath circulation in DC electric arc furnace*, Journal of Iron and Steel Research, International, 13(5), 2006, pp. 7 – 13.

16. Alexis J., Ramirez M., Trapaga G. and Jönsson P., *Modeling of a DC electric arc furnace – heat transfer from the arc*, ISIJ International, Vol. 40, 2000, pp. 1089 – 1097.

17. Coulson, J.M., Richardson, J.F., Backhurst, J.R. and Harker, J.H., *Coulson and Richardson's chemical engineering*, Vol. 1 - Fluid flow, heat transfer and mass transfer ,6th Edition, Elsevier, 1999.

18. Bejan, Adrian and Kraus, Allan D., *Heat transfer handbook*, John Wiley & Sons, 2003.

19. Stankevich Yu. A., Timoshpol'skii V. I., Pavlyukevich N. V., German M. G. and Grinchuk P. S., *Mathematical modeling of the heating and melting of the metal charge in an electric-arc steel- making furnace*, Journal of Engineering Physics and Thermophysics, Vol. 82, No. 2, 2009, pp. 221 – 235.

20. Caffery G., Warnica D., Molloy N. and Lee M., *Temperature homogenization in an electric arc furnace steelmaking bath*, Proceedings of the International Conference on CFD in Mineral and Metal Processing and Power Generation, CSIRO 1997. pp. 87 – 99.

21. ANSYS FLUENT Theory and User's Guide, Release 13.0.0, 2010.

22. Shukla A. K., Dmitry R., Volkova O., Scheller P. R. And Deo B., *Cold model investigations of melting of ice in a gas-stirred vessel*, Metallurgical and Materials Transactions B, Vol. 42, 2010, pp. 224 – 235.

23. Szekely J. Chuang Y. K. and Hilnka J. W., *The melting and dissolution of low carbon steels in iron-carbon melts*, Metallurgical and Materials Transactions, Vol. 3, 1972, pp. 2825 – 2833.

24. Sethi G., Shukla A. K., Das P. C. and Deo B., *Theoretical aspects of scrap dissolution in oxygen steelmaking converters*, AISI Tech, 2004.

25. Enrich O., Chuang Y. and Schwerdtfeger K., *The melting of metal spheres involving the initially frozen shells with different material properties*, International Journal of Heat Mass Transfer, Vol. 21, pp. 341 – 349.

26. EL-Kaddah N., Szekely J. and Carlsson G., *Fluid flow and mass transfer in an inductively stirred four-ton melt of molten steel: a comparison of measurements and predictions*, Metallurgical and Materials Transactions B, Vol. 15, 1982, pp. 633 – 640.

27. Sand U., Yang H., Eriksson J. E., Fdhila R. B., *Numerical and experimental study of fluid dynamic features of combined gas and electromagnetic stirring in ladle furnace*, Steel Research international, Vol. 8, No. 6, 2009, pp. 441 – 449.

28. Ganguly S. and Chakpaborty S., *Numerical investigation on role of bottom gas stirring in controlling thermal stratification in steel ladles*, ISIJ International, Vol. 44, No. 3, 2004, pp. 537 – 546.

29. Cloete S. W. P., *A mathematical modeling study of fluid flow and mixing in gas stirried ladles*, Master thesis, Stellenbosch University, 2008.

30. Stål R. and Carlsson C., *Electromagnetic stirring in electric arc furnace*, Innovation in EAF and in steelmaking processes Conference, 2009.